Finite-Size Scaling Theory of Rényi Thermal Entropy for Second-Order, First-Order, and Weakly First-Order Quantum Phase Transitions

Zhe Wang,[1,2,*] Yanzhang Zhu,[1,2,3] Chunhao Guo,[1,2,†] Bin-Bin Chen,[4] Yi-Ming Ding,[1,2,3] Zenan Liu,[5] and Zheng Yan[1,2,‡]

[1]*Department of Physics, School of Science and Research Center for Industries of the Future, Westlake University, Hangzhou 310030, China*
[2]*Institute of Natural Sciences, Westlake Institute for Advanced Study, Hangzhou 310024, China*
[3]*State Key Laboratory of Surface Physics and Department of Physics, Fudan University, Shanghai 200433, China*
[4]*Peng Huanwu Collaborative Center for Research and Education, Beihang University, Beijing 100191, China*
[5]*Department of Physics, South China University of Technology, Guangzhou 510640, China*

(Received 3 February 2026; revised 22 July 2026; accepted 6 October 2026; published 3 November 2026)

Establishing the nature of a quantum phase transition in finite-size simulations—whether continuous, first order, or weakly first order—is a fundamental challenge in quantum many-body computation. The weakly first-order transition is particularly elusive: its anomalously large correlation length invariably mimics a continuous critical point at accessible system sizes, and no unified finite-size scaling theory has existed to distinguish these scenarios under realistic computational constraints. In this work, we address this problem by introducing a finite-size scaling framework based on the Rényi thermal entropy (RTE) and its derivative (DRTE). We derive the finite-size scaling forms for the RTE and DRTE at continuous, first-order, and weakly first-order quantum phase transitions and show that the DRTE isolates the universal contribution of the free energy and strengthens the characteristics of various phase transitions in finite sizes. Using quantum Monte Carlo simulations, we demonstrate accurate data collapse and extraction of critical exponents at $(2+1)$-dimensional $\mathrm{O}(N)$ critical points. Most importantly, the DRTE provides a definitive signature of weakly first-order transitions at visitable sizes—a zero crossing and a double-peak structure—which we observe in the debated deconfined quantum criticality candidates such as the J-Q and SU(8) J_1-J_2 models. Our approach offers a general, order-parameter-agnostic, and numerically efficient diagnostic tool, resolving long-standing ambiguities between continuous and weakly first-order scenarios in the finite-size simulations.

DOI: 10.1103/42kr-81xw

Subject Areas: Quantum Physics, Statistical Physics

I. INTRODUCTION

Quantum phase transitions, associated spontaneous symmetry breaking, and critical behaviors are central concepts in condensed matter and statistical physics [1–3]. The nature of a phase transition is determined by universal contribution in the free energy or its derivatives, as rigorously defined in standard textbooks: a first-order transition is characterized by a discontinuity in the first derivative of the free energy, while a continuous transition involves higher-order derivatives. In principle, an exact analytical calculation of the partition function would allow unambiguous identification of the transition type through these signatures. However, only a handful of systems admit exact solutions, and the vast majority must be studied numerically. In practice, detecting such features in numerical simulations is highly challenging, as it requires extremely high-precision data to resolve the behavior of derivatives—particularly in strongly correlated many-body systems.

A long-standing and fundamental challenge lies in identifying genuine deconfined quantum critical points (DQCPs) beyond the Landau-Ginzburg-Wilson paradigm. This framework describes continuous transitions between incompatible symmetry-breaking phases, such as the antiferromagnetic (AFM) Néel order—where spin symmetry is

*Contact author: wangzhe90@westlake.edu.cn
†Contact author: guochunhao@westlake.edu.cn
‡Contact author: zhengyan@westlake.edu.cn

Published by the American Physical Society under the terms of the Creative Commons Attribution 4.0 International license. Further distribution of this work must maintain attribution to the author(s) and the published article's title, journal citation, and DOI.

broken—and the valence-bond solid (VBS)—where lattice-rotation symmetry is broken [4–6]. Such continuous transitions exhibit unconventional critical behavior and may host emergent symmetries and fractionalized excitations [7–14]. If realized in nature, DQCPs would represent a fundamentally new class of quantum critical phenomena beyond the Landau-Ginzburg-Wilson framework—a discovery of comparable significance to the establishment of the paradigm itself. However, in concrete model realizations, it remains controversial whether candidate DQCPs represent true continuous transitions or are instead weakly first order. Notable examples include nonlinear sigma models with topological terms [15–18], the J-Q models [5,19–23], and other bosonic or fermionic systems [24–27]. The stakes are enormous: resolving this question determines whether we need an entirely new framework for quantum criticality or whether conventional Landau theory, augmented by proximate multicriticality, suffices.

The core difficulty stems from the fact that correlation lengths ξ at these candidate DQCPs are often orders of magnitude longer than the system sizes accessible in simulations—even if the transition is weakly first order rather than genuinely critical. In the regime $L \ll \xi$, a weakly first-order transition is nearly indistinguishable from a true continuous one. Consequently, the observed critical-like behavior closely mimics that of a continuous transition, making definitive discrimination extremely difficult. This phenomenon is understood within a physical picture in which the weakly first-order transition occurs in close proximity to a critical point—though some researchers argue that the underlying criticality is described by a complex conformal field theory (CFT) [18,28–30], while others propose it arises from a multicritical point [31–33]. As a result, in finite-size simulations, weakly first-order transitions near a critical fixed point are nearly indistinguishable from continuous ones. Given current computational limits, reliably distinguishing between these scenarios across accessible system sizes remains a major challenge.

The severity of this obstacle is best appreciated by surveying the existing diagnostic toolkit. Order parameters and Binder cumulants require delicate extrapolation to $L \to \infty$, but the extrapolation itself depends on assumptions about scaling corrections that are precisely what is debated, especially when the target value is close to zero. Entanglement entropy, one of the most sophisticated modern diagnostics, has recently been shown to be cut dependent in ways not under theoretical control [34–36]: several recent works studying the same J-Q models reached the various conclusions from mutually incompatible signals depending on the lattice bipartition [19–21]. In other words, even the state-of-the-art diagnostic yields signals that change character depending on microscopic implementation choices. The common thread is that no existing method offers a binary, cut-independent, parameter-free signature of phase coexistence at weakly first-order transitions.

Crucially, there is currently no unified and effective finite-size scaling theory capable of robustly differentiating second-order and weakly first-order transitions. As a consequence, most numerical studies lack a definitive "smoking-gun" signature for identifying the true nature of the transition. In this work, we address this gap by developing a scaling theory based on the Rényi thermal entropy (RTE) and its derivative (DRTE)—physical observables that naturally cancel the leading analytic background contributions to the free energy, thereby isolating the universal contribution that governs critical behavior. Unlike all existing diagnostics, the DRTE is defined on the full-system partition function $S^{(2)} = -\ln[Z(2\beta)/Z(\beta)^2]$—no subsystem, no cut, no bipartition dependence. Its signatures at a first-order transition (zero crossing and double-peak structure) follow from thermodynamic identities: they are binary, qualitative features that exist if and only if two phases coexist and are impossible at a genuine continuous transition. This requires no fitting, no extrapolation, and no prior knowledge of the order parameter. Moreover, the DRTE exhibits distinct and universal signatures in both first-order and weakly first-order transitions, enabling clear discrimination between different types of quantum phase transitions. In continuous and weakly first-order cases, it allows for the accurate extraction of critical exponents through data collapse, where the extracted exponents in the latter reflect those of the nearest critical fixed point.

We verify these predictions across a broad range of quantum critical systems. For continuous transitions, the RTE and DRTE reproduce the known critical points and correlation-length exponents of the $(2+1)$D O(1), O(2), and O(3) universality classes, while an independent thermal tensor-network calculation for the one-dimensional transverse-field Ising model further demonstrates that the framework is not restricted to quantum Monte Carlo (QMC). For strong first-order transitions, the anisotropic Heisenberg and checkerboard J-Q models confirm the predicted zero crossing, opposite-sign double-peak structure, and first-order finite-size scaling. More importantly, applying the DRTE to the debated J-Q_2 and J-Q_3 models reveals first-order branch-competition signatures coexisting with pseudocritical scaling. In particular, for the J-Q_2 model, these characteristic weakly first-order signatures are already clearly resolved for system sizes $L = 16$–56, precisely in a regime where conventional diagnostics remain strongly ambiguous. We further apply the DRTE to the SU(8) J_1-J_2 model, which recent entanglement-entropy scaling interpreted as exhibiting a continuous deconfined quantum critical point [37]. In contrast, our DRTE results reveal a clear first-order

component, providing new evidence that the transition of the SU(8) J_1-J_2 model is weakly first order. These results not only validate the scaling framework across established universality classes and first-order transitions, but also demonstrate its ability to uncover weakly first-order behavior in challenging DQCP candidates.

Taken together, our results establish the RTE and DRTE as a general, order-parameter-agnostic, bipartition-independent, and numerically efficient framework for characterizing quantum phase transitions. This provides, to our knowledge, the first qualitative resolution of the long-standing DQCP controversy using a definitive, parameter-free diagnostic at currently accessible simulation scales and demonstrates the practical ability of the DRTE to distinguish continuous from weakly first-order behavior deep within the pseudocritical finite-size regime.

II. SECOND-ORDER PHASE TRANSITION

A. Finite-size scaling form

Let us begin with second-order quantum phase transitions. For a quantum phase transition, the inverse temperature should scale as $\beta = cL^z$, where L is the linear system size, z is the dynamical critical exponent, and c is a fixed spacetime aspect ratio. Since temperature is an irrelevant scaling field, the free energy $F = -(1/\beta)\ln Z$ can be replaced by the logarithm of the partition function $\ln Z$ for the purpose of extracting universal contributions.

At a continuous transition, the correlation length diverges, and the free energy acquires a universal contribution. According to the finite-size scaling hypothesis [38,39], any scaling observable Q near the critical point g_c takes the scaling form

$$Q(\Delta g, L, c) = L^{\sigma}\tilde{S}(\Delta g L^{1/\nu}, c), \tag{1}$$

where $\Delta g = g - g_c$, ν is the correlation-length exponent, σ is a scaling power, and $\tilde{S}$ is a universal scaling function. The universal contribution of the free energy is scale invariant ($\sigma = 0$) [38,40]; hence, $\ln Z$ can be decomposed as

$$\ln Z(g, \beta, L) = a(g)\beta L^d + \mathcal{A}_{\text{sub}}(g, L, \beta) + \tilde{S}(\Delta g L^{1/\nu}, c). \tag{2}$$

Here, $a(g)\beta L^d$ is the leading volume-law term and $\mathcal{A}_{\text{sub}}(g, L, \beta) = \beta(a_1(g)L^{d-1} + a_2(g)L^{d-2} + \cdots)$ collects subleading analytic background contributions. The analytic background terms dominate $\ln Z$ and obscure the universal part $\tilde{S}$, making direct numerical detection of critical universalities challenging.

To isolate $\tilde{S}$, we should construct a quantity in which the dominant analytic background contributions cancel. For a quantum phase transition, temperature is an irrelevant scaling field. Along the finite-size scaling trajectory $\beta \sim L^z$, the analytic background is expected to be linear in β at leading order. Evaluating Eq. (2) at inverse temperatures 2β and β and multiplying the latter by two, we obtain

$$\begin{aligned} \ln Z(2\beta) &= 2a(g)\beta L^d + 2\mathcal{A}_{\text{sub}}(g, L, \beta) + \tilde{S}(\Delta g L^{1/\nu}, 2c), \\ 2\ln Z(\beta) &= 2a(g)\beta L^d + 2\mathcal{A}_{\text{sub}}(g, L, \beta) + 2\tilde{S}(\Delta g L^{1/\nu}, c). \end{aligned} \tag{3}$$

Then, the analytic background cancels, leaving

$$2\ln Z(\beta) - \ln Z(2\beta) = 2\tilde{S}(\Delta g L^{1/\nu}, c) - \tilde{S}(\Delta g L^{1/\nu}, 2c). \tag{4}$$

In the present work, the aspect ratio is fixed to $c = 1$, so the right-hand side depends only on the scaling variable $x = \Delta g L^{1/\nu}$. For convenience, we define the combined universal scaling function

$$\tilde{S}(\Delta g L^{1/\nu}) \equiv 2\tilde{S}(\Delta g L^{1/\nu}, c) - \tilde{S}(\Delta g L^{1/\nu}, 2c), \tag{5}$$

evaluated at $c = 1$, so that

$$2\ln Z(\beta) - \ln Z(2\beta) = \tilde{S}(\Delta g L^{1/\nu}). \tag{6}$$

This identifies the combination $2\ln Z(\beta) - \ln Z(2\beta)$ as the quantity that isolates the universal critical contribution. In Appendix D, within the framework of a low-energy effective theory, we prove—based on the CFT tower—that this difference indeed captures only the universal critical part of the free energy.

The above derivation shows that the difference $2\ln Z(\beta) - \ln Z(2\beta)$ isolates the universal part $\tilde{S}$ through an cancellation of the analytic background. This result admits a transparent physical interpretation within the path-integral formalism: for dynamic exponent $z = 1$, the system exhibits spacetime isotropy (emergent Lorentz invariance), placing imaginary time β and spatial size L on an equal footing. Specifically, Eq. (6) measures the free-energy difference between two Euclidean spacetime manifolds whose temporal circumferences are 2β and β (see Fig. 1). In close analogy with the ordinary Casimir effect [41–47], the finite temporal circumference of the smaller block acts as a "sieve" for critical fluctuations: a larger circumference accommodates a broader modes, while tightening the temporal extent squeezes out soft (long-wavelength) modes at a cost in free energy (see Fig. 1). We call this contribution the *spacetime Casimir effect*. It is dominated by infrared modes and yields an O(1) universal scaling function $\tilde{S}(\Delta g L^{1/\nu})$ (see Appendix E for details).

From an information-theoretic perspective, the combination appearing in Eq. (4) is precisely the second-order Rényi thermal entropy—also known as the purity—a fundamental quantity in information theory [48–54]:

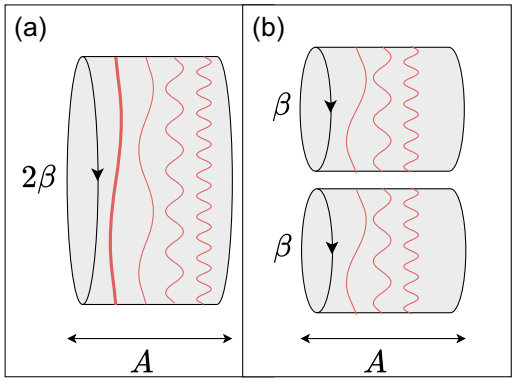


FIG. 1. A geometrical presentation of two partition functions of the whole system (A) (a) $Z(2\beta) = \mathrm{Tr}(e^{-2\beta H})$ and (b) $Z(\beta) = \mathrm{Tr}(e^{-\beta H})$, where H is the Hamiltonian of the system. Near a quantum critical point with dynamical exponent $z = 1$, the system possesses emergent Lorentz invariance, which puts the imaginary time β and the spatial size L on the same footing ($\beta \propto L$). The Rényi thermal entropy then compares the free energies of two Euclidean spacetime blocks whose temporal circumferences are 2β and β, respectively. In close analogy with the ordinary Casimir effect [41–46], the finite imaginary-time circumference β acts as a "sieve" for critical fluctuations (different modes are depicted by red wavy lines of varying wavelengths): a larger circumference admits a broader modes, and the resulting difference in free energy can be understood as the energy cost of excluding long-wavelength (thick red wavy lines) modes when the temporal extent is reduced. We term this universal difference, which is entirely dominated by long-wavelength modes, the *spacetime Casimir effect*.

$$S^{(2)} = -\ln\frac{Z(2\beta)}{Z(\beta)^2}. \tag{7}$$

This definition extends to arbitrary order n as $S^{(n)} = [1/(1-n)]\ln[Z(n\beta)/Z(\beta)^n]$. For simplicity, we focus on the second-order Rényi thermal entropy ($n = 2$) throughout this work.

The above analysis shows that the RTE is a dimensionless quantity dominated by long-wavelength fluctuations. Its scaling dimension is, therefore, $\sigma = 0$ in Eq. (1), and it inherits the scaling form

$$S^{(n)}(\Delta g, L) = \tilde{S}(\Delta g L^{1/\nu}). \tag{8}$$

Differentiating Eq. (8) yields the scaling behavior of the DRTE:

$$\frac{\partial S^{(n)}(\Delta g, L)}{\partial \Delta g} = \tilde{S}'(\Delta g L^{1/\nu}) L^{1/\nu}, \tag{9}$$

where $\tilde{S}'(x) = \partial\tilde{S}(x)/\partial x$ and the factor $L^{1/\nu}$ arises from the derivative of the scaling variable $x = \Delta g L^{1/\nu}$ with respect to Δg.

The above analysis implies two characteristic signatures: (i) the RTE is dimensionless and, therefore, exhibits a crossing at the critical point, analogous to the Binder ratio; (ii) the DRTE allows the critical exponent ν to be extracted through data collapse. To verify these predictions, we expand the scaling function as a polynomial, $\tilde{S}(x) = \sum_{k=0}^{k_{\max}} (1/k!)\tilde{S}^{(k)}(0)x^k$, and perform a global fit to the RTE and DRTE data. In the following, we demonstrate perfect data collapse near the well-established $(2+1)$D O(1) (Z_2), O(2), and O(3) quantum critical points. The critical point g_c, the correlation-length exponent ν, and the expansion coefficients $\tilde{S}^{(k)}(0)$ are treated as fitting parameters; we use $k_{\max} = 6$ throughout the numerical analysis.

B. Numerical methods

The RTE can be expressed in terms of the ratio of partition functions at two different temperatures: $S^{(2)} = -\ln\{[Z(2\beta)]/[Z(\beta)^2]\}$. We compute the partition functions using the bipartite reweight-annealing algorithm [55–57] in combination with stochastic series expansion (SSE) QMC simulations [39,58–62]. Following a method analogous to that used for the derivative of Rényi entanglement entropy and negativity [55,63], the derivative of the RTE with respect to a general parameter g of the Hamiltonian H is given by

$$\frac{dS^{(n)}}{dg} = \frac{1}{1-n}\left[-n\beta\left\langle\frac{dH}{dg}\right\rangle_{Z(n\beta)} + n\beta\left\langle\frac{dH}{dg}\right\rangle_{Z(\beta)}\right]. \tag{10}$$

Here, the two expectation values are evaluated separately using ensembles corresponding to $Z(n\beta)$ and $Z(\beta)$, respectively. While the RTE is calculated using the reweight-annealing QMC method [64–66], the DRTE is directly obtained from the two expectation values in Eq. (10); see Appendix A for details. Considering the dynamical critical exponents $z = 1$ of the models studied in this work, the $\beta = L$ is set to approach the quantum critical regime.

C. Ising transition

We study the bilayer Ising-Heisenberg model with a $(2+1)$D Ising QCP [67]. The Hamiltonian is given by

$$H = -J_z \sum_{\alpha=1,2}\sum_{\langle ij\rangle} S^z_{i,\alpha}S^z_{j,\alpha} + J\sum_i \mathbf{S}_{i,1}\cdot\mathbf{S}_{i,2}, \tag{11}$$

where $\langle ij\rangle$ denotes the nearest-neighbor interaction and $\alpha = 1, 2$ labels the two layers. $-J_z < 0$ represents the intralayer ferromagnetic (FM) Ising interaction, while $J > 0$ represents the interlayer antiferromagnetic (AFM) Heisenberg interaction. For $J/J_z \ll 1$, the ground state exhibits $\mathbb{Z}_2$ symmetry-breaking Ising order. In the opposite limit, $J/J_z \gg 1$, the system forms interlayer spin-singlet states. The QCP separating two phases is at $J/J_z = 3.045(2)$ and belongs to the $(2+1)$D Ising universality class [67].

We set $J = 3.045$ and use J_z as the tuning parameter, studying the second-order RTE and DRTE near the QCP at

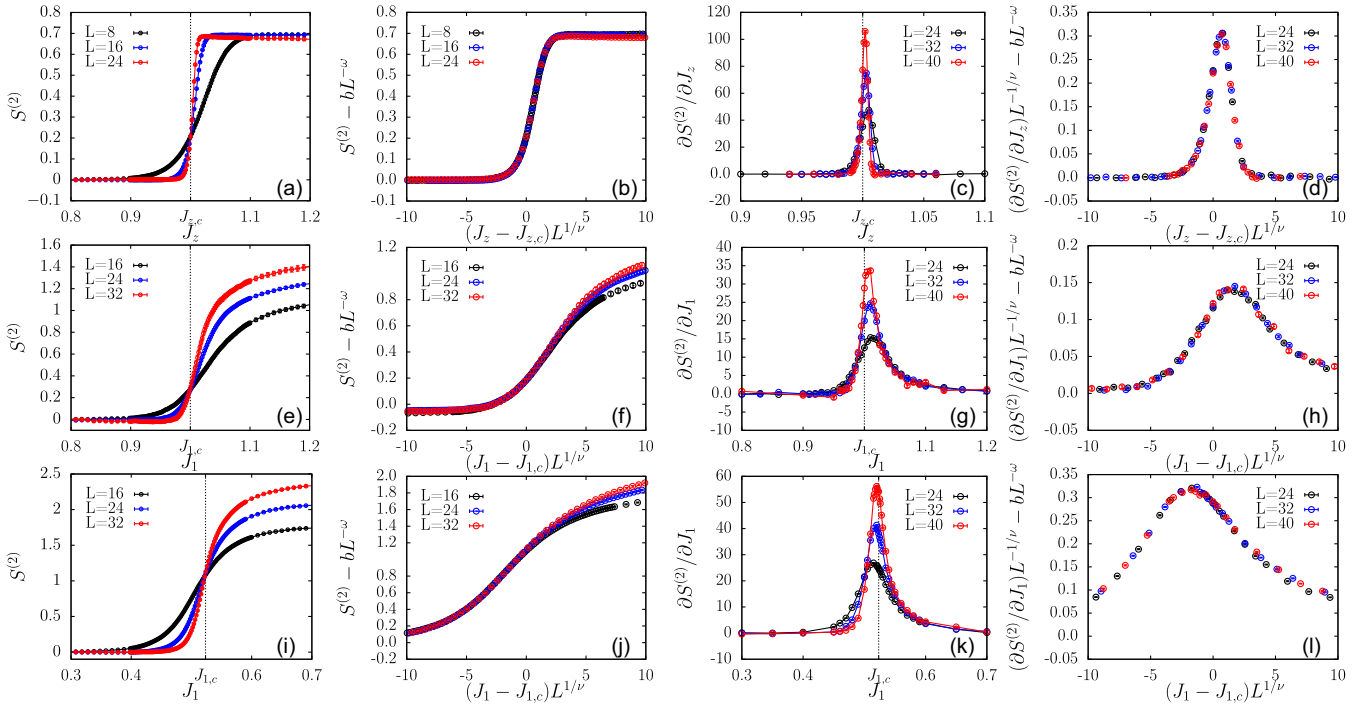


FIG. 2. (a),(c) Second-order RTE and its derivative DRTE and (b),(d) corresponding data collapse analysis near the QCP of the bilayer Ising-Heisenberg model [$(2+1)$D Ising universality]. We set $J = 3.045$ and take J_z as the tuning parameter. (e)–(h) Results for the dimerized anisotropic Heisenberg model with $\Delta = 0.9$ [$(2+1)$D O(2) universality], using $J_2 = 2.1035$ and tuning J_1. (i)–(l) Results for the dimerized isotropic Heisenberg model with $\Delta = 1$ [$(2+1)$D O(3) universality], using $J_2 = 1$ and tuning J_1. To achieve good data collapse, we include a subleading correction: $Q(g, L) = L^k\{\tilde{S}[(g - g_c)L^{1/\nu}] + bL^{-\omega}\}$. $\omega = 0.830$, 0.789, and 0.782 correspond to the $(2+1)$D Ising, O(2), and O(3) critical points, respectively [70–73]. For $Q = S^{(2)}$, $k = 0$. $k = 1/\nu$ when Q is DRTE.

$J_{z,c} = 1$ for various lattice sizes. The results are shown in Figs. 2(a) and 2(c). The RTE curves for different system sizes intersect at the QCP, while the DRTE exhibits a clear peak at the critical point. We fit the scaling forms in Eqs. (8) and (9) to the RTE and DRTE data, respectively. The fits yield $J_{z,c} = 0.9999(1)$, $\nu = 0.629(7)$ from RTE and $J_{z,c} = 1.000(3)$, $\nu = 0.63(4)$ from DRTE. These values are in agreement with the known QCP $J_{z,c} = 1$ [67] and the $(2+1)$D Ising universality class value $\nu = 0.63012$ [67–69]. The resulting universal scaling functions $\tilde{S}(\Delta g L^{1/\nu})$ and $\tilde{S}'(\Delta g L^{1/\nu})$ with $\Delta g = J_z - J_{z,c}$, obtained from data collapse, are displayed in Figs. 2(b) and 2(d), respectively.

D. Continuous symmetry phase transitions

We then investigate QCPs of the dimerized AFM Heisenberg model [74–76]. The Hamiltonian reads

$$H = J_1 \sum_{\langle ij \rangle} D_{ij} + J_2 \sum_{\langle ij \rangle'} D_{ij}, \tag{12}$$

in which $J_2 > J_1 > 0$ and $D_{ij} = S_i^x S_j^x + S_i^y S_j^y + \Delta S_i^z S_j^z$ represents the nearest-neighbor AFM Heisenberg interaction with anisotropy parameter Δ. In the regime where $J_2/J_1 \simeq 1$, the ground state exhibits AFM order. For $0 < \Delta < 1$, the AFM order parameter lies in the xy plane, breaking the O(2) symmetry. For $\Delta > 1$, the order parameter aligns along the z axis, breaking the $\mathbb{Z}_2$ spin flip symmetry. When $\Delta = 1$, the interaction is isotropic, and the AFM order breaks the O(3) symmetry. In the limit $J_2/J_1 \gg 1$, the ground state is the gapped dimer phase. The QCP from the gapped phase to the AFM order belongs to the $(2+1)$D O(2), Ising, and O(3) universality class when $0 < \Delta < 1$, $\Delta > 1$, and $\Delta = 1$, respectively [74–76]. For a zero-temperature system with ground-state degeneracy d_e, the RTE actually reflects the logarithmic degeneracy: $S^{(2)} = \ln d_e$. As shown in Fig. 2, $S^{(2)}$ effectively probes both the degeneracy of discrete symmetry-breaking phases and the Anderson tower of states associated with continuous symmetry breaking [12,77,78].

We evaluate the RTE and its derivative near the QCPs for both the easy-plane case [$\Delta = 0.9$, O(2) criticality] and the isotropic case [$\Delta = 1$, O(3) criticality], with results shown in Figs. 2(e), 2(g), 2(i), and 2(k), respectively. In each case, J_2 is fixed and J_1 is tuned across the transition, as detailed in the caption. Similar to the Ising case, the RTE curves for different system sizes intersect at the QCPs, and their derivatives exhibit clear peaks at these points. We apply the scaling forms in Eqs. (8) and (9) to data near the $(2+1)$D O(2) and O(3) QCPs. For the O(2) QCP, fitting the RTE

yields $J_{1,c} = 0.997(1)$, $\nu = 0.67(2)$, while the DRTE gives $J_{1,c} = 0.9994(8)$, $\nu = 0.66(1)$. These values are consistent with the known critical parameters $J_{1,c} = 1$ and $\nu = 0.6703$ [68,76].

For the O(3) QCP, fitting the RTE data yields $J_{1,c} = 0.523(1)$, $\nu = 0.703(7)$, while the DRTE gives $J_{1,c} = 0.525(1)$, $\nu = 0.708(8)$. These values are consistent with the known critical parameters $J_{1,c} = 0.52337$ and $\nu = 0.7073$ [68,74,75]. The universal scaling functions near the O(2) and O(3) QCPs, obtained from data collapse, are shown in Figs. 2(f), 2(h), 2(j), and 2(l), respectively.

In summary, all the data show that the RTE does have a crossing at a critical point and the DRTE does extract the critical exponent ν by data collapse, which is highly consistent with our theoretical analysis.

III. FIRST-ORDER PHASE TRANSITION

A. Finite-size scaling form

At a zero-temperature first-order transition, two thermodynamic branches have equal energy density at the transition but different generalized-force densities. We write the finite-size energies of the two branches as

$$E_\alpha(g,L) = L^d e_\alpha(g) + E_\alpha^{\mathrm{sub}}(g,L), \qquad \alpha = 1,2, \tag{13}$$

where $e_\alpha(g)$ denotes the leading energy density of branch α while $E_\alpha^{\mathrm{sub}}(g,L)$ collects subextensive corrections. At the transition point,

$$e_1(g_c) = e_2(g_c), \qquad \ell = \partial_g[e_2(g) - e_1(g)]_{g=g_c} \neq 0. \tag{14}$$

Here, ℓ is the jump in the generalized-force density. For a strong first-order transition, intrabranch excitations remain gapped. In the low-temperature coexistence window,

$$Z_\alpha(n\beta) = d_\alpha \mathrm{e}^{-n\beta E_\alpha(g,L)}\left[1 + \mathcal{O}\left(\mathrm{e}^{-n\beta\Delta_\alpha}\right)\right], \tag{15}$$

where d_α is a finite multiplicity and $\Delta_\alpha > 0$ is an intrabranch gap. Neglecting exponentially small interface and intrabranch corrections, the partition function can be approximated as a sum of contributions from the two coexisting branches [79]:

$$Z(n\beta,g,L) \simeq d_1 \mathrm{e}^{-n\beta E_1(g,L)} + d_2 \mathrm{e}^{-n\beta E_2(g,L)}. \tag{16}$$

Define the energy difference between the two branches as

$$\Delta E(g,L) = E_2(g,L) - E_1(g,L), \qquad y = \beta\Delta E(g,L). \tag{17}$$

Factoring out branch 1, the partition function becomes

$$Z(n\beta) = \mathrm{e}^{-n\beta E_1}[d_1 + d_2 \mathrm{e}^{-ny}]. \tag{18}$$

The common branch-1 exponential cancels from the RTE, giving the two-branch expression

$$S^{(n)}(y) = \frac{\ln(d_1 + d_2\mathrm{e}^{-ny}) - n\ln(d_1 + d_2\mathrm{e}^{-y})}{1-n}. \tag{19}$$

At the branch crossing ($y = 0$),

$$S^{(n)}(0) = \ln(d_1 + d_2). \tag{20}$$

Thus, the RTE itself does not vanish at a first-order transition; in the nondegenerate two-branch case, it equals $\ln 2$ at coexistence.

The probability of branch 2 in the $n\beta$ ensemble is described by a logistic function

$$p_n(y) = \frac{d_2\mathrm{e}^{-ny}}{d_1 + d_2\mathrm{e}^{-ny}}, \qquad n > 0. \tag{21}$$

Differentiating Eq. (19) and using $\partial_g y = \beta\partial_g\Delta E(g,L)$, we obtain the DRTE for general n:

$$\partial_g S^{(n)} = \frac{n}{n-1}\partial_g y[p_n(y) - p_1(y)]. \tag{22}$$

For $n = 2$, this reduces to the compact expression

$$\partial_g S^{(2)} = 2\beta\partial_g\Delta E(g,L)[p_2(y) - p_1(y)]. \tag{23}$$

Using Eq. (13) and retaining the leading volume-law term, *the most important result in this section—the key scaling form of the first-order transition—is obtained:*

$$\partial_g S^{(2)} = 2\beta L^d \Delta e'(g)[p_2(y) - p_1(y)] + \cdots, \qquad \Delta e = e_2 - e_1, \tag{24}$$

which immediately explains three characteristic features of the DRTE at a first-order transition.

(i) Since $\Delta e'(g_c) = \ell \neq 0$, the difference $p_2(y) - p_1(y)$ changes sign across g_c [near g_c, $y \approx \beta L^d \ell(g - g_c)$, crossing zero linearly], resulting in a *robust double-peak structure* with one positive and one negative peak located on opposite sides of the transition. This structure reflects the rapid transfer of thermodynamic weight between the two competing branches and is a direct consequence of phase coexistence.

(ii) At the first-order transition point ($y = 0$), since $p_n(0) = p_1(0) = [d_2/(d_1 + d_2)]$, thus

$$\partial_g S^{(2)}|_{\Delta e=0} = 0. \tag{25}$$

The DRTE crosses through 0 at the first-order transition point. For unequal multiplicities, the occupation at coexistence is not generally $1/2$; the zero follows because the β and $n\beta$ ensembles

have the same branch occupation at the exact branch-energy crossing. This represents another fundamental distinction from continuous phase transitions, where the DRTE scales as $L^{1/\nu}$ without a generic zero crossing.

(iii) Because $|p_2(y) - p_1(y)|$ is an O(1) constant and $\Delta e'(g)$ is also of constant order, the peak amplitude of the DRTE scales as

$$\left|\partial_g S^{(2)}\right| \sim \beta L^d \sim L^{d+z_\beta}. \tag{26}$$

Here, z_β denotes the power with which the inverse temperature is increased along the thermal trajectory $\beta = cL^{z_\beta}$ $(c > 0)$. At a first-order transition, there need not be a universal dynamical exponent; z_β is a chosen scaling parameter.

The thermal rounding window is $|y| = O(1)$, which gives

$$\delta g \sim L^{-(d+z_\beta)}, \qquad \left|\partial_g S^{(2)}\right|_{\text{peak}} \sim L^{d+z_\beta}. \tag{27}$$

Consequently, the DRTE satisfies the finite-size scaling ansatz

$$\partial_g S^{(2)} = L^{d+z_\beta} f(\Delta g L^{d+z_\beta}; d_2/d_1) + \cdots. \tag{28}$$

To maintain consistency with the formalism of continuous phase transitions, we can define $1/\nu = d + z_\beta$ for this discontinuity scaling. However, this definition does not imply a diverging correlation length or the existence of a universal first-order dynamical exponent. The divergence of the DRTE does not arise from a critical universality; rather, it stems from the system's intrinsic volume-law scaling and the fact that the free energies of the coexisting phases become unequal once the system moves away from the transition point (see Appendix F for the more detailed derivation).

B. Numerical demonstration

Our numerical simulations confirm our theoretical derivation. Specifically, we study the 2D anisotropic Heisenberg model and the 2D checkerboard J-Q model with first-order transitions [80]. Let us begin by examining the 2D anisotropic Heisenberg model defined in Eq. (12), where the antiferromagnetic couplings are uniform, $J_1 = J_2 = 1$, and the anisotropy parameter Δ serves as the tuning variable. At $\Delta = 1$, the system exhibits full spin-rotation symmetry, corresponding to O(3), which is spontaneously broken by the emergence of AFM order in the ground state. When Δ deviates from unity, the symmetry is explicitly lowered to in-plane spin rotation symmetry and spin-flip symmetry. For $0 < \Delta < 1$, the ground state develops an easy-plane AFM order, spontaneously breaking the continuous SO(2) symmetry. In contrast, for $\Delta > 1$, the system favors an easy-axis AFM order, leading to the breaking of the discrete $\mathbb{Z}_2$ spin-inversion symmetry. Precisely at $\Delta = 1$, both types of order coexist, and each vanishes discontinuously across the transition. This abrupt change in the order parameters signals a first-order quantum phase transition, accompanied by the spontaneous breaking of an enhanced O(3) symmetry [80].

The DRTE across the transition at $\Delta_c = 1$ is shown in Fig. 3(a). A clear discontinuity is observed near the phase transition point, with the DRTE diverging toward opposite signs on either side of the transition in the thermodynamic limit $(L \to \infty)$. For comparison, we also compute the

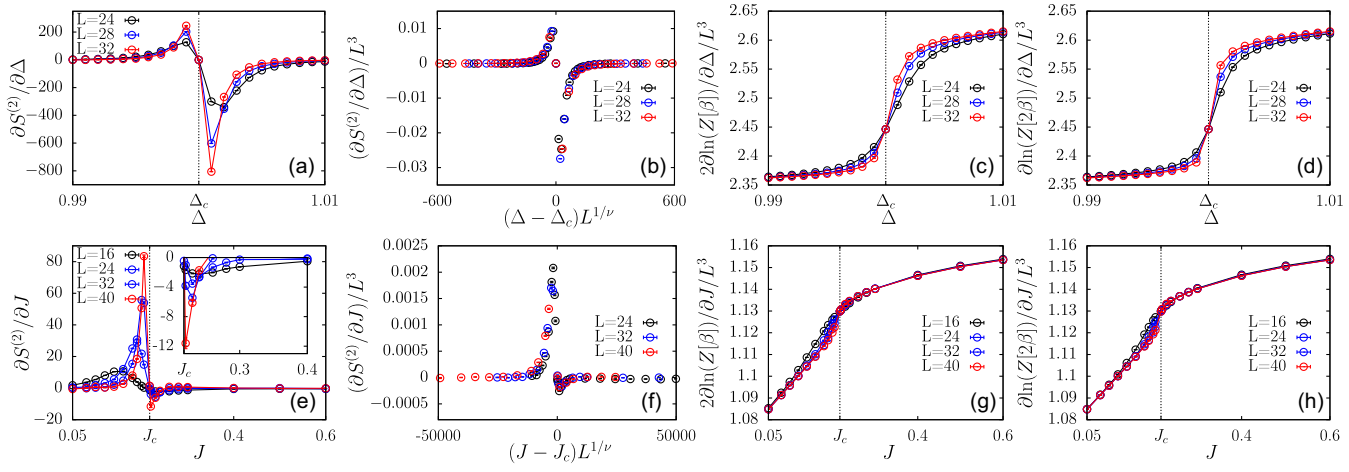


FIG. 3. (a) Derivative of the RTE and (b) corresponding data collapse analysis near the phase transition point of the 2D anisotropic Heisenberg model with anisotropy parameter Δ [see Eq. (12)]. (c) and (d) show the data for the derivative of the partition function at temperatures β and 2β near the transition. Here, $J_1 = J_2 = 1$, and the anisotropy Δ is taken as the tuning parameter. (e)–(h) Results for the checkerboard J-Q model, using $Q = 1$ and tuning J.

derivative of the logarithm of the partition function, as displayed in Figs. 3(c) and 3(d). These curves exhibit a significantly smoother behavior across the transition compared to the DRTE. Moreover, the DRTE curves for different system sizes are seen to intersect precisely at the critical point $\Delta_c = 1$, and the value at the crossing point is zero—consistent with the expected vanishing of the DRTE at a first-order transition. Finally, as shown in the data collapse in Fig. 3(b), the DRTE obeys the scaling form given by Eq. (28). These results provide strong numerical confirmation of our theoretical predictions.

The occurrence of a symmetry-enhanced first-order transition is not limited to systems with exact symmetries. An emergent enhanced symmetry can arise at long wavelengths provided that all explicit symmetry-breaking perturbations are irrelevant under the renormalization group (RG) and, thus, decay along the RG flow. In this scenario, we study the 2D checkerboard J-Q model (see Appendix B for model details), which exhibits a spontaneously broken emergent O(4) symmetry at the first-order transition point $J_c/Q = 0.217(1)$, where the system transitions from an O(3)-symmetry-breaking antiferromagnetic order to a $\mathbb{Z}_2$-symmetry-breaking plaquette-singlet solid order [80]. The DRTE across this transition is shown in Fig. 3(e). A clear discontinuity is observed at the critical point, with the DRTE diverging to opposite signs on either side of the transition in the thermodynamic limit ($L \to \infty$). The DRTE equals zero at the transition point. Furthermore, the DRTE data collapse successfully onto a single curve when rescaled according to Eq. (28) [Fig. 3(f)], consistently confirming the validity of our theoretical predictions. Similar to the anisotropic Heisenberg model, the derivative of the logarithm of the partition function [shown in Figs. 3(g) and 3(h)] exhibits a much smoother behavior across the transition compared to the DRTE.

Combining theoretical analysis with numerical simulations, we demonstrate that the DRTE not only is effective for characterizing continuous phase transitions, but also serves as a powerful probe for first-order phase transitions.

IV. WEAKLY FIRST-ORDER TRANSITIONS

A. Finite-size scaling form

Having established the universal behaviors at continuous and strong first-order transitions, we now turn to weakly first-order transitions, which pose significant challenges for conventional local observables. The fundamental difficulty is that the correlation length at the transition, although finite, is much larger than the accessible system sizes ($L \ll \xi$). In this regime, the renormalization-group flow can remain close to a nearby critical fixed point for many decades in length scale, and observables display pseudocritical scaling with effective exponents ν and z controlled by that nearby critical point—even though the thermodynamic transition is first order [28,29].

In the standard first-order DRTE, quantum fluctuations were neglected because intrabranch excitations are gapped. For a weakly first-order transition, however, the proximity of a critical point introduces strong quantum fluctuations that must be properly accounted for. The finite-size spectrum, therefore, contains two ingredients simultaneously: two competing macroscopic branches and low-energy tower corrections inherited from the nearby scaling regime. Let $\alpha = 1, 2$ label the two branches and m label the low-energy tower attached to branch α. In the critical region of the nearby critical point, the branch-resolved energies take the form

$$E_{\alpha m}(g, L) = L^d e_\alpha(g) + L^{-z}\varepsilon_{\alpha m}(x) + \cdots, \qquad x = (g - g_c)L^{1/\nu}, \tag{29}$$

where $\varepsilon_{\alpha m}(x)$ is a dimensionless scaling function that encodes the low-energy finite-size level m of branch α inherited from the nearby critical regime. At inverse temperature $\beta = cL^z$, the restricted partition function of each branch is

$$Z_\alpha(n\beta) = \mathrm{e}^{-n\beta L^d e_\alpha(g)} Q_\alpha(nc, x), \qquad Q_\alpha(nc, x) = \sum_m \mathrm{e}^{-nc\varepsilon_{\alpha m}(x)} + \cdots, \tag{30}$$

where the tower factor $Q_\alpha(nc, x)$ is O(1) along the finite-size trajectory. The full two-branch partition function is, therefore,

$$Z(n\beta) \simeq \mathrm{e}^{-n\beta L^d e_1(g)} Q_1(nc, x) + \mathrm{e}^{-n\beta L^d e_2(g)} Q_2(nc, x). \tag{31}$$

Unlike in the strong first-order limit, the tower factors Q_α cannot, in general, be treated as constants, because each competing branch retains low-energy spectral weight inherited from the nearby critical fixed point. Consequently, the DRTE combines the branch-occupation response characteristic of a first-order transition with the finite-size response of the pseudocritical tower. After factoring out the common extensive reference energy, and provided that the residual branch-independent tower contribution is negligible or has been subtracted, *the leading DRTE of a weakly first-order transition can be written in the compact form*

$$\frac{\partial S^{(2)}}{\partial g} = \left[2cL^{d+z_\beta}\Delta e'(g) + \tilde{S}'(x)L^{1/\nu}\right][p_2(y) - p_1(y)] + \cdots, \tag{32}$$

where the prime means the derivative versus g. A detailed derivation and the conditions underlying this expression are given in Appendix G.

Equation (32) is the central result for weakly first-order transitions. It predicts three characteristic features.

(i) The *double-peak structure* of a first-order transition is preserved even when the transition is weak, since the occupation difference $p_2(y) - p_1(y)$ remains.

(ii) The *DRTE is 0 at the finite-size coexistence point*, where $p_2(0) = p_1(0) = d_2/(d_1 + d_2)$. This zero crossing is the same thermodynamic identity as in the strong first-order case.

(iii) For accessible system sizes $L \ll \xi$, the coefficient $\Delta e'(g)$ is parametrically small because the two branches are nearly degenerate near the nearby critical fixed point. Consequently, the DRTE does not follow the L^{d+z_β} scaling characteristic of a strong first-order transition; instead, it exhibits $L^{1/\nu}$ pseudocritical scaling inherited from the nearby critical point. When $L \gg \xi$, however, the finite correlation length cuts off the critical fluctuations of a nearby critical fixed point, and the DRTE crosses over to the L^{d+z} scaling of a standard first-order transition.

In the following, we present numerical data that strongly support the analysis above.

B. Finite-size advantage and range of validity

We now clarify why the DRTE can reveal the first-order component of a weakly first-order transition at relatively small system sizes, and the finite-size regime in which this diagnosis is controlled. The favorable finite-size behavior of the DRTE has two complementary physical origins.

First, the Rényi construction suppresses a large smooth contribution to the partition function before any finite-size fitting is performed. Schematically, the logarithm of the partition function can be written as

$$\ln Z(\beta, g, L) = \beta E_{\mathrm{reg}}(g, L) + \mathcal{U}(\beta, g, L) + \delta\mathcal{A}(\beta, g, L), \tag{33}$$

where $E_{\mathrm{reg}}(g, L)$ denotes the dominant smooth contribution that is extensive in the imaginary-time direction, $\mathcal{U}$ contains the nontrivial long-wavelength finite-size contribution, and $\delta\mathcal{A}$ represents remaining subleading corrections. The regular contribution may contain the spatial expansion

$$E_{\mathrm{reg}}(g, L) = a_0(g)L^d + a_1(g)L^{d-1} + a_2(g)L^{d-2} + \cdots. \tag{34}$$

In the Rényi combination,

$$S^{(n)} = \frac{1}{1-n}[\ln Z(n\beta) - n \ln Z(\beta)], \tag{35}$$

the contribution that is linear in the imaginary-time extent cancels identically. Therefore, the large smooth background common to the two thermal partition functions is strongly suppressed, making the remaining long-wavelength finite-size structure more directly visible. This cancellation does not imply that all finite-size corrections disappear: corrections from irrelevant operators, branch-dependent low-energy spectra, and other subleading terms can remain.

Second, once two competing thermodynamic branches contribute appreciably to the finite-size partition function, the DRTE directly probes the redistribution of their statistical weights between the β and $n\beta$ ensembles. As shown by the two-branch description above [Eq. (32)], the occupation difference $p_2(y) - p_1(y)$ changes sign across the branch crossing and vanishes at the finite-size coexistence point. This directly generates the zero crossing and opposite-sign double-peak structure. For a weakly first-order transition, these first-order occupation signatures can coexist with the pseudocritical $L^{1/\nu}$ scaling inherited from the nearby critical fixed point. The combination of background suppression and direct sensitivity to branch redistribution explains why the first-order component can become visible in the DRTE even while other observables remain dominated by critical-like finite-size behavior.

These mechanisms follow from the structure of the Rényi construction and are not specific to the particular models studied here. However, they do not imply that arbitrarily small systems are sufficient. The numerical size at which the characteristic DRTE structure becomes clearly resolvable remains model dependent.

Indeed, the scaling theory developed above is a low-energy effective description and, therefore, requires a separation between the long-wavelength degrees of freedom controlling the transition and microscopic short-distance excitations. Along the finite-size trajectory

$$\beta = cL^z, \tag{36}$$

a low-energy excitation with

$$\Delta_{\mathrm{IR}}(L) \sim L^{-z} \tag{37}$$

satisfies

$$\beta\Delta_{\mathrm{IR}} = \mathrm{O}(1) \tag{38}$$

and, therefore, remains active in the finite-size partition function. By contrast, a microscopic excitation has a finite energy scale Δ_{UV} and contributes with a Boltzmann factor

$$e^{-\beta\Delta_{\mathrm{UV}}} = e^{-cL^z\Delta_{\mathrm{UV}}}. \tag{39}$$

For sufficiently large L,

$$\beta\Delta_{\mathrm{UV}} = cL^z\Delta_{\mathrm{UV}} \gg 1, \tag{40}$$

so that these microscopic excitations are strongly suppressed. Equivalently, in space one requires $L \gg a$, where a is the microscopic lattice scale.

We denote by L_{min} the model-dependent crossover scale beyond which this low-energy separation of scales becomes effective. Schematically, its physical meaning is set by the conditions

$$cL^z\Delta_{\mathrm{UV}} \gg 1, \qquad L/a \gg 1. \tag{41}$$

The scale L_{min} is not universal: it depends on the ultraviolet energy scale, lattice cutoff, irrelevant couplings, and other short-distance details. It is also physically distinct from the correlation length ξ. The former characterizes the crossover from microscopic physics to the low-energy effective regime, whereas the latter characterizes the eventual departure from pseudocritical behavior toward the asymptotic first-order regime.

For a weakly first-order transition with an anomalously large correlation length, these two scales naturally define an intermediate window

$$L_{\mathrm{min}} \ll L \ll \xi. \tag{42}$$

The lower inequality ensures that microscopic high-energy contributions are sufficiently suppressed for the low-energy scaling theory to apply, whereas the upper inequality keeps the system in the pseudocritical regime controlled by the nearby critical fixed point. It is precisely in this window that the DRTE can simultaneously display pseudocritical $L^{1/\nu}$ scaling and the zero-crossing, double-peak structure associated with first-order branch competition.

If $L \lesssim L_{\mathrm{min}}$, microscopic and low-energy physics are still strongly mixed. Short-range lattice-dependent contributions can distort the scaling function, shift or round the zero crossing, and obscure the double-peak structure. A weakly first-order transition may therefore resemble a continuous transition at such small sizes. Importantly, the absence of a first-order DRTE signature in this regime should be regarded as inconclusive rather than as evidence for a continuous transition. This limitation is not specific to the DRTE: in conventional finite-size analyses of order parameters, correlation functions, Binder cumulants, and susceptibilities, the smallest system sizes are likewise excluded when microscopic corrections prevent a stable scaling description.

Thus, the finite-size advantage of the DRTE is a general physical mechanism, whereas the numerical crossover scale at which this advantage becomes visible is model dependent. In the following, we show that the smooth partition-function responses remain nearly featureless while the DRTE already resolves the characteristic first-order branch structure.

C. Numerical demonstration

The phase transition between AFM Néel order and VBS phase in 2D quantum magnets can appear (approximately) continuous, which is thought as the deconfined quantum criticality (DQC) [4,81]. J-Q_2 and J-Q_3 models are prototypical examples that realize such transitions in 2D quantum spin systems [5,22]. These models are free of the sign problem, making them ideal for QMC simulations. Extensive QMC studies have shown that the phase transitions of the J-Q models on the 2D lattice are continuous and exhibit emergent SO(5) symmetry, which is a hallmark of DQC [5,9,22,82–84]. However, the critical exponents observed in these models do not satisfy the conformal bootstrap bounds expected for the SO(5) critical point [85]. Recent works have increasingly suggested that this DQC scenario may instead correspond to a weakly first-order transition [18,19,21,31,37,86–92]. Next, we show that the DRTE behaviors provide a clear and direct signature that the transitions in the J-Q_2 and J-Q_3 models (see Appendix B for models' details) are indeed weakly first order in finite sizes (up to $L = 56$). The observed DRTE signals fully align with the three key features predicted in the previous subsection, offering compelling evidence against a genuine continuous transition.

The transition points of the 2D square lattice J-Q_2 and J-Q_3 models have been numerically determined as $J_c/Q = 0.04502$ and $J_c/Q = 0.67046$, respectively [5,22,31,93]. The DRTE results for both models are shown in Figs. 4(a) and 4(e), along with the derivatives of the logarithmic partition function in Figs. 4(c), 4(d), 4(g), and 4(h). The derivative of the logarithmic partition function appears smooth across the transition, even for large system sizes, as seen in Figs. 4(c) and 4(d) for J-Q_3 and Figs. 4(g) and 4(h) for J-Q_2 model. This shows that the almost smooth derivative of the logarithmic partition function cannot directly reveal the weakly first-order nature, as discussed above, since the logarithmic partition function contains large analytic background contributions.

In contrast, the DRTE reveals clear discontinuities with a double-peak character near the transition points [see Figs. 4(a) and 4(e)], as the feature (i) we predicted in the above subsection. Moreover, DRTE curves for different system sizes intersect at zero at the transition point [as the feature (ii) we predicted above], unlike in continuous phase transitions. These two features are fully consistent with our previous analysis of the DRTE at weakly and standard first-order transitions. Our results demonstrate that the DRTE can unambiguously detect the first-order nature of weakly first-order phase transitions in relatively small systems (up to $L = 56$), even in the J-Q_2 model with much stronger finite-size effects. In fact, its nature, whether continuous or first order, remains under debate so far [31].

We now verify our third theoretical prediction for weakly first-order transitions. We first attempted to scale the DRTE data according to Eq. (28), assuming standard first-order

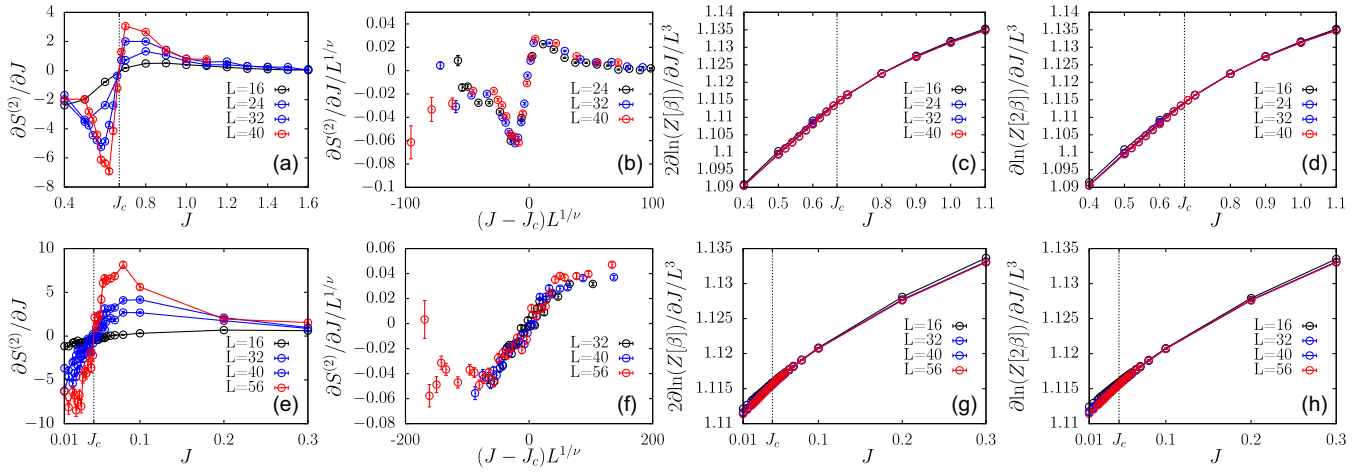


FIG. 4. We set $Q=1$ and use J as the tuning parameter. (a) The derivative of the RTE: DRTE $\partial S^{(2)}/\partial J$. (b) Corresponding data collapse analysis of (a). (c) and (d) show the data for the derivative of the partition function at temperatures β and 2β near the transition of the J-Q_3 model. (e)–(h) Data for the J-Q_2 model. The raw values of the partition function derivative vary significantly across system sizes (see Appendix B), making direct comparison difficult. To resolve this, we normalize the data by L^3, corresponding to $\beta L^2 = L^3$.

scaling. However, we found that the data from different system sizes do not collapse onto a single curve, indicating the inadequacy of this scaling form. We then turned to the modified scaling ansatz for weakly first-order transitions, given by Eq. (32), using the initially estimated deconfined quantum critical exponent $\nu = 0.78$ [5]. Remarkably, for both the J-Q_2 and J-Q_3 models, excellent data collapse is achieved when this form is applied [see Figs. 4(b) and 4(f)]. This scaling behavior is fully consistent with the theoretical expectations discussed in the previous subsection—particularly feature (iii)—and provides strong evidence that the transitions exhibit the characteristic physics of a weakly first-order process, dominated by proximity to a nearby critical point.

It is worth noting that, in current studies based on local order parameters, the observed behavior within accessible system sizes is predominantly governed by signatures of continuous phase transitions, making it difficult to unambiguously identify the underlying first-order nature. As a concrete comparison, the Binder cumulant for the J-Q_2 model shows no negative values even up to $L = 256$, and the spin and dimer correlation functions measured up to $L = 384$ do not display a clear tendency to converge to finite constants (see Appendix J for details); the computational cost of reaching $L = 384$ is roughly 300 times that of $L = 56$. In stark contrast, our DRTE already provides a definitive, qualitative signature of the weakly first-order transition at $L = 56$. This provides a clear and compelling demonstration of the weakly first-order character of the transition, marking, to our knowledge, the first such identification achieved at modest system sizes.

As an additional test, we apply the same DRTE diagnostic to the square-lattice SU(8) J_1-J_2 model, with the detailed results presented in Appendix I. Recent smooth-boundary entanglement-entropy scaling was interpreted as being compatible with a continuous deconfined quantum critical point in this model [37]. In contrast, our DRTE data exhibit a clear sign-changing structure with a zero crossing and opposite-sign extrema near the transition, while the same data simultaneously admit a pseudocritical scaling collapse with an effective exponent $\nu = 0.67(4)$. Within the framework developed above, this coexistence of critical-like finite-size scaling and first-order branch-competition signatures is characteristic of a weakly first-order transition. The SU(8) J_1-J_2 model, therefore, provides an additional nontrivial application of the DRTE, showing that it can reveal a first-order component in a case where other finite-size probes have been interpreted as being consistent with continuous critical behavior.

V. CONCLUSION AND DISCUSSIONS

We have established a unified scaling theory for the RTE and its derivative (DRTE) across all three fundamental types of phase transitions: continuous (second order), strong first order, and weakly first order. Our framework is predicated on the key insight that the DRTE naturally isolates the universal contribution of the free energy by canceling dominant analytic background contributions. Crucially, we have derived distinct and diagnostic scaling behaviors for the DRTE in each regime.

(i) *Continuous phase transitions*—The DRTE scales as

$$\frac{\partial S^{(2)}}{\partial g} = L^{1/\nu}\tilde{S}'(\Delta g L^{1/\nu}), \tag{43}$$

where ν is the correlation length exponent. This allows for precise determination of the critical point g_c and exponent ν via data collapse, as demonstrated for $(2+1)$D O(N) universality classes.

(ii) *Standard first-order transitions*—The DRTE exhibits a characteristic discontinuity with a double-peak structure and follows the volume-law scaling

$$\partial_g S^{(2)} = L^{d+z_\beta} f(\Delta g L^{d+z_\beta}; d_2/d_1) + \cdots, \quad (44)$$

where d is the spatial dimension and z_β is a chosen scaling parameter (at a first-order transition, there need not be a universal dynamical exponent). The zero crossing at g_c and the sign change of the peaks provide an unambiguous signature of phase coexistence.

(iii) *Weakly first-order transitions*—The DRTE obeys a hybrid scaling form

$$\frac{\partial S^{(2)}}{\partial g} = \left[2cL^{d+z_\beta}\Delta e'(g) + \tilde{S}'(x)L^{1/\nu}\right] \times [p_2(y) - p_1(y)] + \cdots, \quad (45)$$

which encapsulates the competition between the underlying first-order mechanism (first term) and the influence of a nearby critical fixed point (second term). In accessible finite sizes ($L \ll \xi$), the critical-like $L^{1/\nu}$ scaling dominates, explaining the observed data collapse with continuous exponents. Simultaneously, the persistent double-peak structure and zero crossing betray the first-order nature, as conclusively shown for the debated J-Q models.

Our numerical results establish this framework at two complementary levels. First, the well-established O(1), O(2), and O(3) quantum critical points and the strong first-order anisotropic Heisenberg and checkerboard J-Q transitions provide controlled benchmarks for the continuous- and first-order scaling theories. Second, the J-Q_2, J-Q_3, and SU(8) J_1-J_2 models constitute nontrivial applications where the transition character is considerably more subtle. In all three cases, the DRTE reveals the coexistence of pseudocritical scaling and first-order branch-competition signatures. In particular, the result of SU(8) J_1-J_2 model indicates weakly first-order behavior even though recent smooth-boundary entanglement-entropy scaling was interpreted as being compatible with a continuous transition [37]. These results, therefore, go beyond benchmark confirmation of the scaling theory and demonstrate its ability to uncover previously unresolved first-order components in candidate deconfined quantum critical systems.

Beyond these specific findings, the RTE-DRTE approach offers a general and order-parameter-agnostic diagnostic tool. Its applicability extends to transitions elusive to conventional local observables, including potential topological phase transitions. While validated here with high-precision quantum Monte Carlo, our method is readily adaptable to other numerical techniques. As a concrete demonstration, we have implemented our scaling framework within the thermal tensor network method for the one-dimensional transverse-field Ising model, successfully extracting the critical point and exponent ν in agreement with exact results (see Appendix K for details) [92,94]. This work, thus, provides a new paradigm for characterizing quantum criticality, resolving the long-standing challenge of distinguishing weakly first-order from continuous transitions in finite-size simulations.

ACKNOWLEDGMENTS

We thank the helpful discussions with Cheng-Xiang Ding, Yan-Cheng Wang, Menghan Song, Zi Yang Meng, Chong Wang, and Wenan Guo. Z. W. was supported by the National Natural Science Foundation of China under Grants No. 12605078 and by the China Postdoctoral Science Foundation under Grant No. 2024M752898. This project is supported by the Scientific Research Project (No. WU2025B011), Feng-Ying Career Development Chair Fund and the Start-up Funding of Westlake University, and the Natural Science Foundation of China (Grant No. 12674188), and Quantum MetaKey (QuaMeK) computing. The authors thank the IT service office and the high-performance computing center of Westlake University.

Z. W. and Y. Z. contributed equally to this work.

DATA AVAILABILITY

There are no publicly available research data or software supporting this manuscript. Requests for further information or data should be sent to the authors.

APPENDIX A: METHOD

The nth-order Rényi entropy is defined as $S^{(n)} = [1/(1-n)]\ln \mathrm{Tr}(\rho^n)$ [or $[1/(1-n)]\ln \mathrm{Tr}(\rho_A^n)$], where $\rho = e^{-\beta H}/Z$ and $Z = \mathrm{Tr}e^{-\beta H}$ (with H being the Hamiltonian). Here, $\rho_A = \mathrm{Tr}_B\rho$ represents the reduced density matrix of subsystem A coupled with an environment B. The Rényi entanglement entropy is defined using ρ_A, while the RTE is based on ρ. In this work, we focus on RTE. From the above definitions, it is evident that the Rényi entropy can be expressed as the ratio of partition functions at two different temperatures: $S^{(n)} = [1/(1-n)]\ln\{[Z(n\beta)]/Z(\beta)^n\}$ (for simplicity, we consider $S^{(2)}$ in this work).

The partition functions can be calculated using the bipartite reweight-annealing algorithm [55,64,65,95] in conjunction with SSE QMC simulations [39,58–62]. The key idea is to transform the problem of solving the ratio of partition functions with different parameter into the problem of reweighting:

$$\frac{Z(J')}{Z(J)} = \left\langle \frac{W(J')}{W(J)} \right\rangle_{Z(\beta,J) \text{ or } Z(n\beta,J)}, \tag{A1}$$

where the $\langle \cdots \rangle_{Z(\beta,J) \text{ or } Z(n\beta,J)}$ indicates that the QMC samplings is performed under the manifold $Z(\beta, J)$ or $Z(n\beta, J)$ at parameter J (note parameter J is a physical parameter here). $W(J')$ and $W(J)$ represent the weights of a same configuration but under different parameters J' and J, respectively.

In this frame, we can designed the incremental process along the path composed of real physical parameters. In other words, all intermediates are physical partition functions at corresponding parameters. The continuously incremental trick here are introduce as follows:

$$\frac{Z(J')}{Z(J)} = \prod_{i=0}^{N-1} \frac{Z(J_{i+1})}{Z(J_i)}, \tag{A2}$$

where $J_N = J'$ and $J_0 = J$, other J_i locate between the two in sequence. In realistic simulation, we are able to gain any ratio $Z(J')/Z(J)$ in this way. But $Z(n\beta, J')/Z^n(\beta, J')$ cannot be obtained. The antidote comes from some known reference point $Z(n\beta, J)/Z^n(\beta, J)$: assuming that we have calculated the ratios $Z(n\beta, J')/Z(n\beta, J)$ and $Z(\beta, J')/Z(\beta, J)$ using the method described above, the ratio $Z(n\beta, J')/Z^n(\beta, J')$ can be obtained if $Z(n\beta, J)/Z^n(\beta, J)$ is known. For a given zero-temperature phase, and assuming the ground-state degeneracy is d_e, one can derive that $S^{(n)} = [1/(1-n)] \ln\{[Z(n\beta)]/Z^n(\beta)\} = \ln de$. Therefore, we can use states with known degeneracies—such as dimer product states (with degeneracy 1 in this work) and discrete symmetry-breaking states (with degeneracy 2 in this work)—as reference points at a given parameter J. In this way, $Z(n\beta, J)/Z^n(\beta, J)$ can be determined by solving $[1/(1-n)] \ln\{[Z(n\beta, J)]/Z^n(\beta, J)\} = \ln de$.

One might be concerned about how to deal with a Hamiltonian without a state with known degeneracy. In this way, we can introduce a temperature axis starting from infinite temperature and annealing down to the target temperature. The degeneracy at infinite temperature is known as 2^N (consider an N-spin system with spin 1/2).

The RTE derivative of J is

$$\frac{dS^{(n)}}{dJ} = \frac{1}{1-n} \left[\frac{dZ(n\beta)/dJ}{Z(n\beta)} - n \frac{dZ(\beta)/dJ}{Z(\beta)} \right]. \tag{A3}$$

According to $Z(\beta) = \mathrm{Tr} e^{-\beta H}$, we have

$$\frac{dZ}{dJ} = \mathrm{Tr}\left[-\beta \frac{dH}{dJ} e^{-\beta H} \right]. \tag{A4}$$

Thus,

$$\frac{dZ/dJ}{Z} = -\beta \left\langle \frac{dH}{dJ} \right\rangle_Z. \tag{A5}$$

Similarly, we can obtain

$$\frac{dZ(n\beta)/dJ}{Z(n\beta)} = -n\beta \left\langle \frac{dH}{dJ} \right\rangle_{Z(n\beta)}. \tag{A6}$$

Therefore, the RTE derivative can be rewritten as

$$\frac{dS^{(n)}}{dJ} = \frac{1}{1-n} \left[-n\beta \left\langle \frac{dH}{dJ} \right\rangle_{Z(n\beta)} + n\beta \left\langle \frac{dH}{dJ} \right\rangle_Z \right]. \tag{A7}$$

The equations above is general and does not depend on detailed QMC methods. Then let us discuss how to calculate them in SSE simulation. For convenience, we fix the Rényi index $n = 2$ and choose the dimerized Heisenberg model in the main text as the example for explaining technical details. The Hamiltonian is

$$H = J_1 \sum_{\langle ij \rangle} S_i S_j + J_2 \sum_{\langle ij \rangle} S_i S_j. \tag{A8}$$

In the following, we fix $J_2 = 1$ and leave J_1 as the tunable parameter. Note the Hamiltonian is a linear function of J_1; that means $dH/dJ_1 = H_{J_1}/J_1$ in which H_{J_1} is the J_1 term in Hamiltonian. Then, the RTE derivative can be simplified as

$$\frac{dS^{(2)}}{dJ_1} = \left[2\beta \left\langle \frac{H_{J_1}}{J_1} \right\rangle_{Z(2\beta)} - 2\beta \left\langle \frac{H_{J_1}}{J_1} \right\rangle_Z \right]. \tag{A9}$$

In the SSE frame, it is easy to obtain $\langle H \rangle = \langle -n_{op}/\beta \rangle$ [96], where n_{op} is the number of the concerned Hamiltonian operators. Thus, the Eq. (A9) can be further simplified to

$$\frac{dS^{(2)}}{dJ_1} = \left[-\left\langle \frac{n_{J_1}}{J_1} \right\rangle_{Z(2\beta)} + 2 \left\langle \frac{n_{J_1}}{J_1} \right\rangle_Z \right], \tag{A10}$$

where n_{J_1} means the number of J_1 operators including both diagonal and off-diagonal ones. It is worth noting that there is no "2" anymore in the $\langle \cdots \rangle_{Z(2\beta)}$ term, because n_{J_1} here contains two replicas' operators which has already been doubled actually.

Note that the RTE is computed using the reweight-annealing QMC method mentioned above, while the DRTE is obtained directly by separately evaluating the two expectation values involved in Eq. (A9) or (A10). This implies that the computational cost of evaluating DRTE is roughly twice that of energy calculations. Typically, we perform on the order of one million Monte Carlo steps when computing the energy, and we have adopted the same number of steps in the present study.

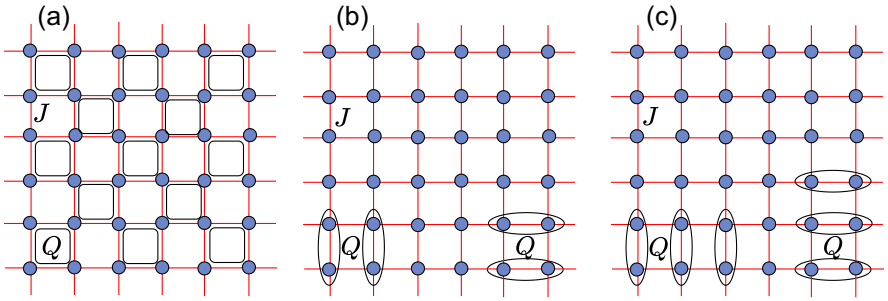


FIG. 5. J-Q models, in which the antiferromagnetic Heisenberg interaction (J term) acts on all nearest-neighbor bonds. (a) The checkerboard J-Q model on a square lattice with periodic boundary condition in both directions. The four-spin interaction (Q term) acts on nearest-neighbor bond pairs that form a plaquette. (b) J-Q_2 model: the four-spin Q interaction covers the entire lattice. (c) J-Q_3 model: the six-spin Q interaction covers the entire lattice.

APPENDIX B: J-Q MODELS

In this work, we studied three types of J-Q models, namely, checkerboard J-Q, J-Q_2, and J-Q_3 models. The Hamiltonian of the checkerboard J-Q model on a square lattice is given by [80]

$$H = -J\sum_{\langle ij\rangle} P_{ij} - Q\sum_{[ijkl]} P_{ij}P_{kl}, \tag{B1}$$

where $P_{ij} = 1/4 - \mathbf{S}_i \cdot \mathbf{S}_j$ denotes the projection operator onto the singlet state of spins at sites i and j. The first term sums over all nearest-neighbor bond pairs $\langle ij\rangle$, while the second term runs over plaquettes composed of two parallel bonds (ij) and (kl), as illustrated in Fig. 5(a). J-Q_2 and checkerboard J-Q models share the same Hamiltonian form, except that in the J-Q_2 [5] model the Q interactions span the entire lattice, as illustrated in Fig. 5(b). Compared to the J-Q_2 model, the Q interactions

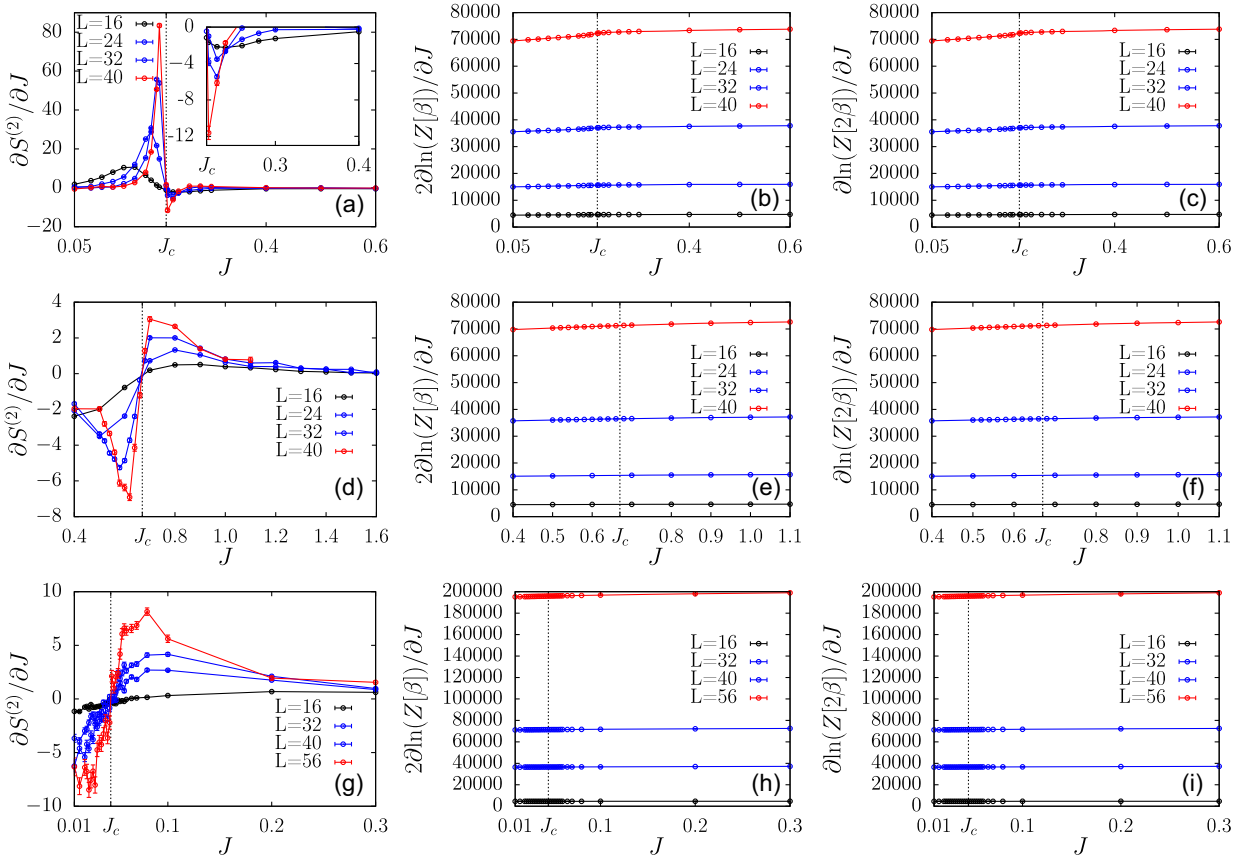


FIG. 6. We set $Q = 1$ and use J as the tuning parameter. (a) The derivative of the RTE: DRTE $\partial S^{(2)}/\partial J$. An inset shows the data on the right side of the phase transition point. (b) and (c) show the data for the derivative of the partition function at temperatures β and 2β near the transition of the checkerboard J-Q model. (d)–(f) Data for the J-Q_3 model. (g)–(i) Data for the J-Q_2 model.

in the J-Q_3 model are composed of the product of three singlet operators [22]:

$$H = -J\sum_{\langle ij\rangle} P_{ij} - Q\sum_{[ijklmn]} P_{ij}P_{kl}P_{mn}, \tag{B2}$$

as illustrated in Fig. 5(c). The DRTE results for three models are shown in Fig. 6, along with the derivatives of the logarithmic partition function in Figs. 6(b), 6(c), 6(e), 6(f), 6(h), and 6(i).

APPENDIX C: DEFINITIONS, THERMAL PROTOCOL, AND EXACT IDENTITIES

We consider a finite quantum system of linear extent L in d spatial dimensions, governed by a Hamiltonian $H(g)$ that depends smoothly on a tuning parameter g. Its partition function and normalized thermal density matrix are

$$Z(\beta, g, L) = \mathrm{Tr}\, e^{-\beta H(g)}, \qquad \rho(\beta, g, L) = \frac{e^{-\beta H(g)}}{Z(\beta, g, L)}. \tag{C1}$$

The order-n thermal Rényi entropy is [48]

$$\begin{aligned} S^{(n)}(\beta, g, L) &= \frac{1}{1-n}\ln \mathrm{Tr}\rho^n \\ &= \frac{\ln Z(n\beta, g, L) - n\ln Z(\beta, g, L)}{1-n}. \end{aligned} \tag{C2}$$

For $n = 2$,

$$S^{(2)} = 2\ln Z(\beta) - \ln Z(2\beta) = -\ln\frac{Z(2\beta)}{Z(\beta)^2}. \tag{C3}$$

Thus, $e^{-S^{(2)}} = \mathrm{Tr}\rho^2$ is the purity, while $S^{(2)}$ is its negative logarithm. Because the RTE is defined for the full thermal density matrix, it introduces neither a spatial bipartition nor an entangling surface. This convention also fixes the sign of the partition-function difference:

$$\ln Z(2\beta) - 2\ln Z(\beta) = -S^{(2)}. \tag{C4}$$

If $\mathcal{L}(x, c)$ denotes the universal contribution to $\ln Z$, the corresponding entropy scaling function is $2\mathcal{L}(x, c) - \mathcal{L}(x, 2c)$. In the residual-free-energy convention $\mathcal{F}_{\mathrm{crit}} = -\mathcal{L}$, the same quantity is $\mathcal{F}_{\mathrm{crit}}(x, 2c) - 2\mathcal{F}_{\mathrm{crit}}(x, c)$. Throughout Appendixes D and E, $\tilde{S}_n$ denotes this RTE scaling function rather than a contribution to $\ln Z$.

With the convention in Eq. (C3), the left-hand sides of main-text Eqs. (4) and (6) equal $-S^{(2)}$, whereas their right-hand sides follow the sign convention for $S^{(2)}$. Identifying those equations with the RTE, therefore, requires one overall sign reversal. All expressions below use $S^{(2)}$ and $\partial_g S^{(2)}$ as defined in Eqs. (C3) and (C10). A global sign reversal changes the orientation of the DRTE curve but neither its scaling exponent nor the positions of its zeros.

We compare different system sizes along the thermal trajectory

$$\beta = cL^{z_\beta}, \qquad c > 0. \tag{C5}$$

At a continuous quantum critical point, we set $z_\beta = z$, where z is the dynamical critical exponent. At a first-order transition, z_β is not a universal exponent; it specifies only how the simulation temperature is reduced as L increases. The thermal rounding is then controlled by $\beta L^d \sim L^{d+z_\beta}$ rather than by a correlation-length exponent. The main text uses $c = \beta/L^{z_\beta}$ as the numerical aspect-ratio parameter. For a relativistic critical point with $z_\beta = 1$, the metric-normalized temporal aspect ratio is

$$\rho_\tau = \frac{v\beta}{L} = vc. \tag{C6}$$

The simulations with $\beta = L$, therefore, have $c = 1$ in lattice units, but they are isotropic in spacetime only if the chosen metric normalization gives $v = 1$. Appendix E discusses this distinction in detail.

We define

$$V(g) = \partial_g H(g) \tag{C7}$$

as the generalized force conjugate to g. At fixed L and β, differentiating the trace and using cyclicity gives

$$\partial_g \ln Z(s\beta, g, L) = -s\beta\langle V\rangle_{s\beta}, \qquad s > 0. \tag{C8}$$

This identity does not require H to commute with $\partial_g H$. Differentiating Eq. (C2) then gives

$$\partial_g S^{(n)} = \frac{n\beta}{n-1}\left[\langle V\rangle_{n\beta} - \langle V\rangle_\beta\right]. \tag{C9}$$

For the second RTE,

$$\partial_g S^{(2)} = 2\beta\left[\langle V\rangle_{2\beta} - \langle V\rangle_\beta\right]. \tag{C10}$$

In Eqs. (C9) and (C10), the derivative is taken at fixed β for each finite system. The trajectory $\beta = cL^{z_\beta}$ is imposed only when comparing different sizes.

The RTE is invariant under a common, g-dependent shift of all energy levels. If

$$Z_{\mathrm{ref}}(s\beta, g, L) = e^{-s\beta F_{\mathrm{ref}}(g,L)}, \tag{C11}$$

then

$$\ln Z_{\mathrm{ref}}(n\beta) - n\ln Z_{\mathrm{ref}}(\beta) = 0. \tag{C12}$$

Equivalently, $S^{(n)}$ is unchanged under $H(g) \mapsto H(g) + F_{\mathrm{ref}}(g,L)\mathbf{1}$. This cancellation removes the extensive ground-state energy and any common term strictly linear in the temporal circumference. On the flat, spatially periodic geometries considered here, ultraviolet-local bulk counterterms have precisely this form. It does not remove nonlocal finite-temperature terms, finite-size excitation towers, or any contribution with nontrivial dependence on the temporal aspect ratio.

This cancellation does not extend to a multilevel sector. If

$$Z(s\beta,g,L) = \mathrm{e}^{-s\beta F_{\mathrm{ref}}(g,L)}\mathcal{Q}_s(g,L), \qquad \mathcal{Q}_s = \sum_m \mathrm{e}^{-sc\varepsilon_m}, \tag{C13}$$

then

$$S^{(n)} = \frac{\ln \mathcal{Q}_n - n \ln \mathcal{Q}_1}{1-n}. \tag{C14}$$

Because $\mathcal{Q}_n \neq \mathcal{Q}_1^n$, in general, the finite-size tower gives a physical contribution to the RTE. The distinction between a common single exponential and a common multilevel tower underlies both the critical Casimir construction and the weakly first-order analysis below. The RTE subtraction removes the leading analytic free-energy background without eliminating the universal finite-size response.

APPENDIX D: CONTINUOUS QUANTUM TRANSITIONS: A SINGLE CRITICAL TOWER

At a continuous transition, the infrared flow approaches a real critical fixed point. For fixed geometry and boundary conditions, the low-energy spectrum forms a single finite-size critical tower [38,40,97,98]. The main text denotes the leading $n=2$, $c=1$ entropy scaling function by $\tilde{S}(x)$. Here, we keep the Rényi index and temporal aspect ratio explicit and write $\tilde{S}_n(x,c)$. We define

$$x = (g - g_{\mathrm{c}})L^{1/\nu}, \qquad \beta = cL^z, \tag{D1}$$

where ν and z are the correlation-length and dynamical exponents, respectively. The finite-size levels have the scaling form

$$E_m(g,L) = E_{\mathrm{ref}}(g,L) + L^{-z}\varepsilon_m(x, u_1 L^{-\omega_1}, u_2 L^{-\omega_2}, \ldots) + o(L^{-z}). \tag{D2}$$

Here, E_{ref} is a common analytic reference energy, u_i are irrelevant scaling fields, and $\omega_i > 0$ are correction-to-scaling exponents. The normalization of the dimensionless levels ε_m includes the temporal metric factor. For $z=1$, Eq. (D2) may equivalently be written as

$$E_m(g,L) = E_{\mathrm{ref}}(g,L) + \frac{v}{L}\mathcal{E}_m(x,\ldots) + o(L^{-1}), \tag{D3}$$

so that the Boltzmann factors depend on $\rho_\tau = v\beta/L$. One may either absorb v into $\varepsilon_m = v\mathcal{E}_m$ and use $c = \beta/L$, as in the main text, or retain $\mathcal{E}_m$ and use ρ_τ. These conventions are equivalent but should not be combined within a single formula.

At inverse temperature $s\beta = scL^z$,

$$Z(s\beta,g,L) = \mathrm{e}^{-s\beta E_{\mathrm{ref}}(g,L)}\mathcal{Q}_s(x,L), \qquad \mathcal{Q}_s(x,L) = \sum_m \exp\left[-sc\varepsilon_m(x, u_1 L^{-\omega_1}, \ldots)\right]. \tag{D4}$$

The tower factor admits the correction-to-scaling expansion

$$\mathcal{Q}_s(x,L) = Q_s^{(0)}(x,c) + \sum_i L^{-\omega_i} Q_{s,i}^{(1)}(x,c) + \cdots. \tag{D5}$$

The common exponential in Eq. (D4) cancels from the RTE, whereas the critical tower remains. Thus,

$$S^{(n)}(g,L;c) = \tilde{S}_n(x,c) + \sum_i L^{-\omega_i}\tilde{S}_{n,i}(x,c) + \cdots, \tag{D6}$$

where

$$\tilde{S}_n(x,c) = \frac{\ln Q_n^{(0)}(x,c) - n \ln Q_1^{(0)}(x,c)}{1-n}. \tag{D7}$$

The subscript s denotes the same critical tower evaluated at temporal aspect ratio sc; it does not represent s independent copies of the c geometry. Independent copies enter only through $Z(\beta)^n$ in the denominator of the RTE ratio. This distinction is central to the spacetime construction in Fig. 1.

The same spectral representation has a direct probability interpretation. Introduce

$$p_m(x,c) = \frac{\mathrm{e}^{-c\varepsilon_m(x)}}{Q_1^{(0)}(x,c)}, \qquad \sum_m p_m = 1. \tag{D8}$$

Then,

$$\tilde{S}_n(x,c) = \frac{1}{1-n}\ln \sum_m p_m(x,c)^n. \tag{D9}$$

A common shift $\varepsilon_m \mapsto \varepsilon_m + a(x)$ cancels from Eq. (D9); only the scaled gaps and their finite-aspect-ratio weights enter.

For $n=2$,

$$S^{(2)}(g,L;c) = 2\ln Q_1^{(0)}(x,c) - \ln Q_2^{(0)}(x,c) + \mathcal{O}(L^{-\omega}). \tag{D10}$$

Differentiating Eq. (D6) at fixed L and β gives

$$\partial_g S^{(n)} = L^{1/\nu}\partial_x \tilde{S}_n(x,c) + \sum_i L^{1/\nu-\omega_i}\partial_x \tilde{S}_{n,i}(x,c) + \cdots. \tag{D11}$$

The leading term in Eq. (D11) arises from the relevant scaling field. Smooth g dependence of nonuniversal metric factors, including $v(g)$ in $\rho_\tau = v(g)\beta/L$, generates additional $O(L^0)$ terms at fixed β. These terms are subleading to $L^{1/\nu}$ unless symmetry suppresses the leading derivative. A feature at finite scaling coordinate x_*, therefore, satisfies

$$g_*(L) - g_c = x_* L^{-1/\nu} + \cdots, \qquad \left|\partial_g S^{(n)}\right|_* \propto L^{1/\nu}. \tag{D12}$$

At the bulk critical point,

$$\partial_g S^{(n)}(g_c, L; c) = L^{1/\nu}\partial_x \tilde{S}_n(0,c) + \cdots. \tag{D13}$$

In general, $\partial_x \tilde{S}_n(0,c)$ need not vanish. A DRTE zero at a continuous transition, therefore, requires an additional symmetry or a stationary point of the scaling function; criticality alone does not enforce it.

Because $S^{(n)}$ is dimensionless, curves at fixed aspect ratio approach a common value at $g = g_c$:

$$S^{(n)}(g_c, L; c) = \tilde{S}_n(0,c) + L^{-\omega}\tilde{S}_{n,1}(0,c) + \cdots. \tag{D14}$$

Retaining one irrelevant field for sizes L and bL, and assuming $\partial_x \tilde{S}_n(0,c) \neq 0$, gives the crossing drift

$$g_\times(L) - g_c = C(b)L^{-(1/\nu+\omega)} + \cdots. \tag{D15}$$

If the leading derivative vanishes, the drift is controlled by higher derivatives or subleading correction fields.

Outside the critical window, the limiting RTE is determined by the low-energy spectrum of the phase. A unique gapped ground state gives

$$Z(\beta) \simeq e^{-\beta E_0} \Rightarrow S^{(n)} \to 0, \tag{D16}$$

whereas a thermally unresolved q-fold manifold gives

$$Z(\beta) \simeq q e^{-\beta E_0} \Rightarrow S^{(n)} \to \ln q. \tag{D17}$$

When a continuous symmetry is spontaneously broken, the Anderson tower of states provides an additional contribution [99,100]. For an O(N) order parameter,

$$E_\ell - E_0 = \frac{\ell(\ell+N-2)}{2I_L} + \cdots, \qquad I_L \propto L^d. \tag{D18}$$

If $\beta \propto L^z$ with $d > z$, then $\beta/I_L \to 0$ and

$$Z_{\rm rot}(\beta) \propto \left(\frac{I_L}{\beta}\right)^{(N-1)/2}. \tag{D19}$$

Consequently,

$$S^{(n)}_{\rm rot} = \frac{N-1}{2}(d-z)\ln L + \mathcal{O}(1). \tag{D20}$$

This ordered-phase tower is distinct from the critical tower governing Eqs. (D6) and (D11). The continuous-transition results used in the main text are, therefore, leading finite-size statements at fixed aspect ratio: the RTE approaches a common crossing value up to corrections from irrelevant fields, and the DRTE scales as $L^{1/\nu}$. A single critical tower does not, by itself, enforce either a zero or an opposite-sign two-lobe profile.

APPENDIX E: RESIDUAL FINITE-SIZE FREE ENERGY AND THE SPACETIME CASIMIR PICTURE

1. Residual free energy on a finite Euclidean geometry

Here, "Casimir" refers to the residual, geometry-dependent free energy of a gapless theory on a finite Euclidean manifold after local analytic contributions have been subtracted [41,44,45]. For a geometry $\mathcal{G}_\lambda$ with boundary or periodicity data $\mathcal{B}_\lambda$, write

$$-\ln Z[\mathcal{G}_\lambda, \mathcal{B}_\lambda] = F_{\rm loc}[\mathcal{G}_\lambda, \mathcal{B}_\lambda] + \mathcal{F}_{\rm res}[\mathcal{G}_\lambda, \mathcal{B}_\lambda]. \tag{E1}$$

The local term contains ultraviolet-sensitive integrals of local densities, including bulk-volume contributions and, when present, surface, edge, corner, and counterterm contributions. The residual term is the nonlocal finite-size contribution. In the critical scaling limit, it is universal once the geometry, aspect ratios, boundary conditions, and metric normalization are specified.

Hyperscaling fixes the residual contribution to be O(1) in the finite-aspect-ratio regime [38,97]. The singular free-energy density obeys

$$f_{\rm sing}(g, T, L^{-1}) = b^{-(d+z)} f_{\rm sing}\Big((g-g_c)b^{1/\nu}, Tb^z, L^{-1}b\Big). \tag{E2}$$

Setting $b = L$, $x = (g-g_c)L^{1/\nu}$, and $c = \beta/L^z$ gives

$$f_{\rm sing}(g, T, L^{-1}) = L^{-(d+z)}\mathfrak{f}(x, c^{-1}). \tag{E3}$$

The corresponding dimensionless Euclidean free energy is

$$\beta L^d f_{\rm sing} = c\mathfrak{f}(x, c^{-1}) \equiv \mathcal{F}_{\rm crit}(x, c) = \mathrm{O}(1). \tag{E4}$$

The anomalous dimension η does not enter this power counting: it governs correlation functions, not the scaling dimension of the free-energy density.

Gaplessness is essential. In a unique-ground-state gapped phase, the residual dependence on a macroscopic cycle is exponentially suppressed once the cycle exceeds

the correlation length. At criticality, no finite infrared scale cuts off this dependence, and the residual free energy retains universal information about the full Euclidean geometry.

2. Parallel plates and the compact-cycle analog

The electromagnetic Casimir effect provides the standard reference point [41–43]. For two ideal parallel plates separated by a, the normal momentum is quantized as $k_z = n\pi/a$. After the bulk and surface self-energies are subtracted, the residual vacuum energy and force per unit area in three spatial dimensions are

$$\frac{E_{\mathrm{Cas}}(a)}{A} = -\frac{\pi^2}{720}\frac{\hbar c_0}{a^3},$$
$$\frac{F_{\mathrm{Cas}}(a)}{A} = -\frac{\partial}{\partial a}\frac{E_{\mathrm{Cas}}(a)}{A} = -\frac{\pi^2}{240}\frac{\hbar c_0}{a^4}. \tag{E5}$$

The mechanical force is obtained by differentiating the residual energy with respect to the plate separation. The RTE probes the same infrared mechanism—the dependence of gapless modes on finite geometry—but involves a finite difference of free energies rather than a mechanical derivative.

A more direct spatial analog of the full-system thermal ratio is a theory with one periodic spatial cycle. Let $\mathcal{M}_L$ denote the remaining $d-1$ directions, each of characteristic size L, and consider

$$\mathcal{G}_{\mathrm{sp}}(R) = \mathcal{M}_L \times S^1_R, \qquad \phi(u+R) = \phi(u), \qquad r = R/L. \tag{E6}$$

The allowed momenta are $k_u = 2\pi m/R$. After local terms are removed, write

$$-\ln Z_{\mathrm{sp}}(g, L, R) = \mathcal{F}^{\mathrm{sp}}_{\mathrm{loc}}(g, L, R) + \mathcal{F}^{\mathrm{sp}}_{\mathrm{Cas}}(x, r) + o(1). \tag{E7}$$

The analog of the second-RTE construction compares two independent R cycles with one cycle of circumference $2R$:

$$\mathcal{S}^{\mathrm{sp}}_{2,\mathrm{Cas}}(x, r) = \mathcal{F}^{\mathrm{sp}}_{\mathrm{Cas}}(x, 2r) - 2\mathcal{F}^{\mathrm{sp}}_{\mathrm{Cas}}(x, r) = -\ln\frac{\mathcal{Z}^{\mathrm{sp}}_{\mathrm{Cas}}(x, 2r)}{[\mathcal{Z}^{\mathrm{sp}}_{\mathrm{Cas}}(x, r)]^2}, \tag{E8}$$

where $\mathcal{Z}^{\mathrm{sp}}_{\mathrm{Cas}} = \exp[-\mathcal{F}^{\mathrm{sp}}_{\mathrm{Cas}}]$. A $2R$ circle is not equivalent to an R circle traversed twice. Its mode spacing is π/R, rather than $2\pi/R$, and it, therefore, supports additional long-wavelength modes.

The periodic scalar field makes this power counting explicit. For a massless real scalar with one compact direction and $d-1$ noncompact transverse directions,

$$\frac{E^{\mathrm{per}}_{\mathrm{Cas}}(R)}{V_\perp} = -\frac{\Gamma(\frac{d+1}{2})\zeta(d+1)}{\pi^{(d+1)/2}}\frac{1}{R^d}. \tag{E9}$$

The coefficient depends on the field content and boundary conditions, while dimensional analysis fixes the dependence on R. For $R \sim L$ and $V_\perp \sim L^{d-1}$, the total residual energy scales as L^{-1}. At a relativistic critical point, $\beta \sim L$, and hence $\beta E_{\mathrm{Cas}} = \mathrm{O}(1)$, consistent with Eq. (E4).

3. Temporal compactification and the RTE finite difference

For the full quantum system, the Euclidean manifold is $\Sigma_L \times S^1_\beta$. In the critical scaling regime, write

$$-\ln Z(\beta, g, L) = \beta E_{\mathrm{loc}}(g, L) + \mathcal{F}_{\mathrm{crit}}(x, c) + o(1). \tag{E10}$$

On a smooth periodic spacetime, the local contribution is linear in the temporal circumference and, therefore, cancels from the full-system RTE. Equation (C3) then gives the singular residual contribution

$$S^{(2)}_{\mathrm{sing}}(x, c) = \mathcal{F}_{\mathrm{crit}}(x, 2c) - 2\mathcal{F}_{\mathrm{crit}}(x, c) = -\ln\frac{\mathcal{Z}_{\mathrm{crit}}(x, 2c)}{\mathcal{Z}_{\mathrm{crit}}(x, c)^2} \tag{E11}$$

with $\mathcal{Z}_{\mathrm{crit}} = \exp[-\mathcal{F}_{\mathrm{crit}}]$. More generally,

$$S^{(n)}_{\mathrm{sing}}(x, c) = \frac{\mathcal{F}_{\mathrm{crit}}(x, nc) - n\mathcal{F}_{\mathrm{crit}}(x, c)}{n-1}. \tag{E12}$$

Geometrically, the numerator of the purity contains one smooth thermal cylinder of circumference 2β, while the denominator contains two disconnected cylinders of circumference β. Because the sewing acts on the entire spatial system, it creates neither a spatial entangling surface nor a local codimension-two replica defect. We use "spacetime Casimir effect" for the residual free-energy difference generated by this global change of temporal compactification.

4. Critical tower and cancellation of the ground-state contribution

The same result follows directly from the critical spectrum in Appendix D. With

$$E_m(g, L) = E_{\mathrm{ref}}(g, L) + L^{-z}\varepsilon_m(x) + o(L^{-z}), \tag{E13}$$

we have

$$\mathcal{Z}_{\mathrm{crit}}(x, c) = \sum_m \mathrm{e}^{-c\varepsilon_m(x)}, \qquad \mathcal{F}_{\mathrm{crit}}(x, c) = -\ln \mathcal{Z}_{\mathrm{crit}}(x, c). \tag{E14}$$

Defining $p_m(x,c) = \mathrm{e}^{-c\varepsilon_m}/\mathcal{Z}_{\mathrm{crit}}$ gives

$$S^{(2)}_{\mathrm{sing}}(x,c) = -\ln \sum_m p_m(x,c)^2. \tag{E15}$$

The residual temporal Casimir term is, therefore, the second Rényi entropy of the normalized weights over the universal finite-size tower.

The ground-state Casimir energy alone is not the RTE contribution. Decompose the scaled levels as

$$\varepsilon_m(x) = \varepsilon_0(x) + \delta_m(x), \qquad \delta_0 = 0. \tag{E16}$$

Then,

$$\mathcal{Z}_{\mathrm{crit}}(x,c) = \mathrm{e}^{-c\varepsilon_0(x)}\left[1 + \sum_{m>0}\mathrm{e}^{-c\delta_m(x)}\right],$$
$$\mathcal{F}_{\mathrm{crit}}(x,c) = c\varepsilon_0(x) - \ln\left[1 + \sum_{m>0}\mathrm{e}^{-c\delta_m(x)}\right]. \tag{E17}$$

The term $c\varepsilon_0$ is linear in the temporal circumference and cancels identically in the RTE finite difference:

$$2c\varepsilon_0 - 2(c\varepsilon_0) = 0. \tag{E18}$$

For a nondegenerate ground state, the surviving contribution is

$$S^{(2)}_{\mathrm{sing}}(x,c) = 2\ln\left[1 + \sum_{m>0}\mathrm{e}^{-c\delta_m(x)}\right] - \ln\left[1 + \sum_{m>0}\mathrm{e}^{-2c\delta_m(x)}\right]. \tag{E19}$$

The scaled ground-state Casimir term exhibits the same O(1) power counting as the residual free energy but cancels from the RTE. The surviving finite difference is governed by the finite-aspect-ratio occupation of the excitation tower. A thermally unresolved ground-state degeneracy is incorporated by replacing the leading 1 in Eq. (E19) with the corresponding degeneracy.

5. Matsubara scale, temporal aspect ratio, and the spacetime Casimir picture

We now specialize to the $(2+1)$-dimensional geometries used in the simulations. The full spatial manifold is the periodic $L \times L$ torus

$$\Sigma_L = T^2_L, \tag{E20}$$

and the thermal partition function has the Hamiltonian representation

$$Z_\Sigma(\beta, g, L) = \mathrm{Tr}_{\mathcal{H}(\Sigma_L)}\mathrm{e}^{-\beta H_\Sigma(g,L)}. \tag{E21}$$

Equivalently, it is the Euclidean path integral on

$$T^2_L \times S^1_\beta. \tag{E22}$$

The Hamiltonian trace and the Euclidean path integral are two representations of the same partition function.

At fixed L and g, varying β in Eq. (E21) does not change the eigenvalues of $H_\Sigma(g,L)$; it changes only their Boltzmann weights. At a relativistic critical point, the low-energy levels take the form

$$E_m(g,L) = E_{\mathrm{ref}}(g,L) + \frac{v}{L}\mathcal{E}_m(x) + o(L^{-1}),$$
$$x = (g - g_c)L^{1/\nu}, \tag{E23}$$

where v is the emergent velocity and $\mathcal{E}_m$ denotes dimensionless torus-spectrum data for the chosen geometry and boundary conditions. This is Eq. (E13) with $z = 1$ and $\varepsilon_m = v\mathcal{E}_m$.

To compare imaginary time with a spatial length, the velocity must be included. Introducing the length coordinate

$$y = v\tau, \tag{E24}$$

the circumference of the Euclidean-time cycle is

$$L_\tau = v\beta, \qquad \rho_\tau = \frac{L_\tau}{L} = \frac{v\beta}{L}. \tag{E25}$$

The infrared critical theory, therefore, lives on a three-torus with cycle lengths L, L, and L_τ. The simulation convention

$$\beta = cL \tag{E26}$$

keeps $\rho_\tau = vc$ fixed at criticality. The simulations reported in the main text use $\beta = L$, so $c = 1$ in lattice units and $\rho_\tau = v$. This is a valid fixed-aspect-ratio trajectory, but it is not necessarily an isotropic three-torus. Isotropy in the continuum metric requires $L_\tau = L$, or $\beta = L/v$. Thus, c is the numerical time-to-space ratio used in the main text, whereas universal torus amplitudes depend on the metric-normalized ratio ρ_τ.

The path integral provides the complementary Matsubara description. A bosonic critical field is periodic around the thermal circle and admits the expansion

$$\phi(\tau, \boldsymbol{r}) = \sum_{n\in\mathbb{Z}}\mathrm{e}^{-\mathrm{i}\omega_n\tau}\phi_n(\boldsymbol{r}), \qquad \omega_n = \frac{2\pi n}{\beta}. \tag{E27}$$

In the length coordinate $y = v\tau$, the corresponding temporal wave number is

$$k_{\tau,n} = \frac{\omega_n}{v} = \frac{2\pi n}{v\beta} = \frac{2\pi n}{L_\tau}. \tag{E28}$$

Finite β, therefore, discretizes the frequency direction. The static $n = 0$ sector is present for any circumference, while the smallest nonzero bosonic frequency is $2\pi/\beta$. Shortening the time circle raises this infrared scale and precludes nonconstant temporal variations whose wavelength would exceed the circumference. This kinematic statement remains valid in an interacting critical theory, although the partition function need not factorize into independent oscillator modes.

For the second RTE, the comparison is particularly transparent. On a circle of circumference β,

$$\omega_m^{(\beta)} = \frac{2\pi m}{\beta}, \tag{E29}$$

whereas on a circle of circumference 2β,

$$\omega_n^{(2\beta)} = \frac{\pi n}{\beta}. \tag{E30}$$

Even values $n = 2m$ reproduce the β-circle frequencies, whereas odd values $n = 2m + 1$ fall between them. The longer circle, therefore, admits additional nonzero frequencies between those of the β circle. Both spectra remain unbounded in the ultraviolet: doubling the circumference does not enlarge a microscopic bandwidth but instead refines the infrared frequency grid. Moreover, $Z(\beta)^2$ describes two disconnected copies of the β geometry, not a single circle with twice the mode multiplicity. One 2β circle and two independent β circles, therefore, have different residual free energies.

Figure 1 illustrates this geometric comparison. Figure 1(a) represents the single connected Euclidean cylinder contributing $Z(2\beta)$, and Fig. 1(b) the two disconnected cylinders contributing $Z(\beta)^2$. The label A denotes the complete spatial system; one spatial direction of the actual T_L^2 geometry is suppressed. The arrows indicate periodic tracing in imaginary time.

The red curves are schematic long-wavelength critical fluctuations, not individual many-body eigenstates, and neither their number nor their thickness is quantitative. The thick, slowly varying curve drawn only on the 2β cylinder represents a fluctuation in the additional soft nonzero temporal sector allowed by the smaller spacing in Eq. (E30). Accordingly, the term "sieve" in the main text refers to the infrared quantization of nonzero temporal wavelengths. The "energy cost" in the caption denotes the change in the dimensionless residual free energy $-\ln Z$, not an eigenvalue assigned to a particular curve. Varying β reweights the fixed Hamiltonian spectrum; it does not remove selected microscopic modes.

A dual transfer-matrix channel makes the spatial Casimir analogy explicit. After the rescaling $y = v\tau$, the infrared path integral is defined on the three-torus (L, L, L_τ). One may slice this manifold along a spatial direction rather than along y. With the dual Hamiltonian normalized in physical energy units,

$$Z_\Sigma(\beta, g_c, L) = \mathrm{Tr}_{\mathcal{H}(T^2_{L_\tau,L})} \exp\left[-\frac{L}{v} H_{\mathrm{dual}}(L_\tau, L)\right]. \tag{E31}$$

Equation (E31) is simply another transfer-matrix decomposition of the same critical path integral; it does not introduce a new microscopic model.

For a $(2 + 1)$-dimensional relativistic critical theory on a spatial torus with circumferences L_x and L_y, the finite-size levels have the general form

$$E_m(L_x, L_y) - E_{\mathrm{ref}}(L_x, L_y) = \frac{v}{L_x}\mathcal{E}_m\left(\frac{L_y}{L_x}\right) + o(L_x^{-1}). \tag{E32}$$

Applying this to the dual channel with $L_x = L_\tau = v\beta$ and $L_y = L$ gives

$$E_m^{\mathrm{dual}} - E_0^{\mathrm{dual}} = \frac{1}{\beta}\left[\mathcal{E}_m^{\mathrm{dual}}(\rho_\tau^{-1}) - \mathcal{E}_0^{\mathrm{dual}}(\rho_\tau^{-1})\right] + o(\beta^{-1}). \tag{E33}$$

The dual finite-size gaps and the Matsubara spacing are, therefore, set by the same inverse-time scale, $1/\beta$, up to dimensionless geometry-dependent factors. The kinematic factor 2π in the Matsubara frequencies should not be identified with the interacting torus spectrum. In particular, $E_m - E_0 = (2\pi v/L)\Delta_m$ is specific to a $(1 + 1)$-dimensional CFT quantized on a circle. In $(2 + 1)$ dimensions, the state-operator correspondence maps local operators to states on S^2, not to the spectrum on T^2. Torus levels are universal but depend on the torus shape and boundary conditions.

The Hamiltonian, Matsubara, and dual-channel pictures are mutually consistent. In the Hamiltonian channel, β sets the occupation of the fixed finite-size levels in Eq. (E23). In the Matsubara representation, it fixes the temporal frequency spacing. In the dual channel, $L_\tau = v\beta$ becomes a compact spatial circumference and produces gaps of the order of $1/\beta$. These are three representations of the same geometric dependence of the critical partition function, not separate additive effects.

With the entropy convention of Eq. (C3), the geometry used in the main text gives

$$S^{(2)}(\beta, g, L) = -\ln\frac{Z_\Sigma(2\beta, g, L)}{Z_\Sigma(\beta, g, L)^2}. \tag{E34}$$

After cancellation of the local terms linear in the temporal circumference, the critical residual contribution is

$$S^{(2)}_{\mathrm{sing}}(x, c) = \mathcal{F}_{\mathrm{crit}}(x, 2c) - 2\mathcal{F}_{\mathrm{crit}}(x, c). \tag{E35}$$

For the data in the main text, $c = 1$ and, hence,

$$S^{(2)}_{\rm sing}(x,1) = \mathcal{F}_{\rm crit}(x,2) - 2\mathcal{F}_{\rm crit}(x,1). \tag{E36}$$

In metric-normalized variables, the two terms evaluate the same critical theory at temporal aspect ratios $2v$ and v, respectively. The spacetime Casimir contribution in this work is the finite difference in Eq. (E35), not a mechanical derivative with respect to a plate separation.

The order of limits is essential. At criticality,

$$\Delta_L = E_1 - E_0 = \frac{v}{L}[\mathcal{E}_1(0) - \mathcal{E}_0(0)] + o(L^{-1}), \tag{E37}$$

so, along $\beta = cL$,

$$\beta\Delta_L = cv[\mathcal{E}_1(0) - \mathcal{E}_0(0)] + o(1). \tag{E38}$$

The finite-aspect-ratio limit

$$L \to \infty, \qquad \beta = cL, \qquad c = \mathrm{O}(1), \tag{E39}$$

therefore, retains a finite occupation of the universal critical tower. By contrast, taking $\beta \to \infty$ at fixed L projects onto a unique ground state and gives $S^{(2)} \to 0$. In a unique-ground-state gapped phase with thermodynamic gap $\Delta > 0$, the trajectory $\beta = cL$ yields $\beta\Delta \to \infty$, so the critical residual contribution is exponentially suppressed. This statement applies to the critical Casimir sector: a finite ground-state degeneracy contributes $\ln q$, and a phase with spontaneously broken continuous symmetry may retain the Anderson-tower term discussed in Appendix D.

In this sense, the spacetime Casimir picture is a controlled infrared interpretation of the RTE finite difference: it isolates the universal response of a gapless finite-size spectrum to temporal compactification, without assigning independent microscopic modes to the schematic curves in Fig. 1.

APPENDIX F: FIRST-ORDER QUANTUM TRANSITIONS: TWO GAPPED BRANCHES

1. Two-branch partition function

At a zero-temperature first-order transition, two thermodynamic branches cross in energy density while retaining different generalized-force densities. The standard formula in the main text applies when four conditions hold: the coexistence window is dominated by two branches; each branch has a finite, s-independent multiplicity; intrabranch excitations satisfy $\beta\Delta_\alpha \gg 1$; and tunneling and interface sectors are exponentially suppressed. We write

$$E_\alpha(g,L) = L^d e_\alpha(g) + E^{\rm sub}_\alpha(g,L), \qquad \alpha = 1,2, \tag{F1}$$

with

$$e_1(g_{\rm c}) = e_2(g_{\rm c}), \qquad \ell = \partial_g[e_2(g) - e_1(g)]_{g=g_{\rm c}} \neq 0. \tag{F2}$$

The coefficient ℓ is the discontinuity in the generalized-force density. Because each branch remains gapped, its low-temperature contribution in the coexistence window is

$$Z_\alpha(s\beta) = d_\alpha \mathrm{e}^{-s\beta E_\alpha(g,L)}\left[1 + \mathcal{O}\left(\mathrm{e}^{-s\beta\Delta_\alpha}\right)\right], \tag{F3}$$

where d_α is a finite multiplicity and $\Delta_\alpha > 0$ is the intrabranch gap. Up to exponentially small interface, tunneling, and intrabranch corrections,

$$Z(s\beta,g,L) \simeq d_1 \mathrm{e}^{-s\beta E_1(g,L)} + d_2 \mathrm{e}^{-s\beta E_2(g,L)}. \tag{F4}$$

We define

$$\Delta E(g,L) = E_2(g,L) - E_1(g,L), \qquad y = \beta\Delta E(g,L). \tag{F5}$$

After factoring out branch 1,

$$Z(s\beta) = \mathrm{e}^{-s\beta E_1}[d_1 + d_2 \mathrm{e}^{-sy}]. \tag{F6}$$

The common exponential cancels from the RTE, giving

$$S^{(n)}_{\rm FO}(y) = \frac{\ln\left(d_1 + d_2\mathrm{e}^{-ny}\right) - n\ln\left(d_1 + d_2\mathrm{e}^{-y}\right)}{1-n}. \tag{F7}$$

At the branch-energy crossing,

$$S^{(n)}_{\rm FO}(0) = \ln(d_1 + d_2). \tag{F8}$$

The unshifted RTE of Eq. (C2) is, therefore, finite at coexistence and equals $\ln 2$ for two nondegenerate branches. The sign change occurs in the derivative, not in the entropy itself. A coupling-independent plotting offset leaves the DRTE unchanged, but the shifted quantity is no longer the absolute RTE defined in Eq. (C2).

2. Occupation identity, zero crossing, and finite-size scaling

The occupation probability of branch 2 in the $s\beta$ ensemble is

$$p_s(y) = \frac{d_2\mathrm{e}^{-sy}}{d_1 + d_2\mathrm{e}^{-sy}}, \qquad s > 0. \tag{F9}$$

Differentiating Eq. (F7) gives

$$\partial_g S^{(n)}_{\rm FO} = \frac{n}{n-1}\partial_g y[p_n(y) - p_1(y)]. \tag{F10}$$

For $n = 2$,

$$\partial_g S^{(2)}_{\rm FO} = 2\beta\partial_g\Delta E(g,L)[p_2(y) - p_1(y)]. \tag{F11}$$

Using Eq. (F1),

$$\partial_g S_{\mathrm{FO}}^{(2)} = 2\beta L^d \Delta e'(g)[p_2(y) - p_1(y)] + \cdots, \quad \Delta e = e_2 - e_1. \tag{F12}$$

At $\Delta E = 0$,

$$p_n(0) = p_1(0) = \frac{d_2}{d_1 + d_2}, \qquad \partial_g S_{\mathrm{FO}}^{(n)}|_{\Delta E=0} = 0. \tag{F13}$$

At the branch-energy crossing, the occupations in the $n\beta$ and β ensembles coincide even when $d_1 \neq d_2$, provided the multiplicities are finite constants and the intrabranch spectra are frozen. This should be distinguished from equal occupation within a single $s\beta$ ensemble, which occurs at $sy = \ln(d_2/d_1)$ and, therefore, depends on s. For $y > 0$, branch 2 lies higher in energy and is more strongly suppressed in the colder $n\beta$ ensemble, so $p_n < p_1$; for $y < 0$, the inequality reverses. Because $p_n - p_1$ also vanishes in both pure-phase limits, the DRTE has two lobes of opposite sign. Their orientation depends on the branch labels and on the sign of $\partial_g \Delta E$. Equal multiplicities give an antisymmetric leading line shape, whereas unequal multiplicities skew the lobes without removing the zero at $y = 0$.

Let $g_0(L)$ denote the finite-size branch crossing,

$$\Delta E[g_0(L), L] = 0, \qquad g_0(L) \to g_{\mathrm{c}}. \tag{F14}$$

Near this point,

$$\Delta E(g, L) = L^d \ell_L [g - g_0(L)] + \cdots, \qquad \ell_L \to \ell. \tag{F15}$$

Along $\beta = cL^{z_\beta}$,

$$y = c\ell_L [g - g_0(L)] L^{d+z_\beta} + \cdots. \tag{F16}$$

The thermal coexistence window is defined by $|y| = \mathrm{O}(1)$, which gives

$$\delta g_{\mathrm{FO}} \sim L^{-(d+z_\beta)}, \qquad \left|\partial_g S_{\mathrm{FO}}^{(n)}\right|_{\mathrm{peak}} \sim L^{d+z_\beta}. \tag{F17}$$

The leading finite-size form is

$$\partial_g S_{\mathrm{FO}}^{(n)} = L^{d+z_\beta} \mathcal{F}_n([g - g_0(L)] L^{d+z_\beta}; d_2/d_1) + \cdots. \tag{F18}$$

The notation $1/\nu_{\mathrm{FO}} = d + z_\beta$ is merely a convenient parametrization of discontinuity rounding; it does not imply a diverging correlation length or a universal first-order dynamical exponent.

Subextensive branch energies determine the drift of the finite-size crossing:

$$g_0(L) - g_{\mathrm{c}} = -\frac{E_2^{\mathrm{sub}}(g_{\mathrm{c}}, L) - E_1^{\mathrm{sub}}(g_{\mathrm{c}}, L)}{L^d \ell} + \cdots. \tag{F19}$$

This drift is distinct from the narrower thermal rounding width in Eq. (F17). The exact finite-size zero, therefore, occurs at $g_0(L)$ and need not coincide with the thermodynamic coupling g_{c} at finite L. Constant multiplicities modify the RTE profile but do not shift the zero away from $\Delta E = 0$. If either branch retains an aspect-ratio-dependent low-energy tower, its contribution cannot be reduced to a constant; Appendix G treats that weakly first-order regime.

3. Finite-size tunneling

If the two branches share the same exact quantum numbers, finite-size tunneling can produce an avoided crossing. In the two-branch subspace,

$$H_{\mathrm{eff}} = \bar{E}\mathbf{1} + \frac{\Delta E}{2}\sigma^z + t_L \sigma^x, \qquad \Omega_L = \sqrt{(\Delta E/2)^2 + t_L^2}. \tag{F20}$$

The corresponding partition function is

$$Z(s\beta) = 2\mathrm{e}^{-s\beta\bar{E}} \cosh(s\beta\Omega_L). \tag{F21}$$

At a first-order transition, t_L is typically exponentially small in a positive power of L. Since β grows only algebraically, $\beta t_L \to 0$, and the incoherent two-branch result is recovered, with corrections of the order of $(\beta t_L)^2$ near coexistence. A smooth g dependence of t_L produces corrections of the same exponential order. If the branches belong to different exact symmetry sectors, $t_L = 0$ identically. Interface states and tunneling instantons are likewise exponentially suppressed in the asymptotic two-branch regime. Under these conditions, the zero crossing, the L^{d+z_β} peak scale, and the $L^{-(d+z_\beta)}$ width all follow from the same occupation identity.

APPENDIX G: WEAKLY FIRST-ORDER TRANSITIONS: COEXISTENCE AND PSEUDOCRITICAL TOWERS

A weakly first-order transition is characterized by a finite but potentially very large crossover length $\xi_\star$. For $L \lesssim \xi_\star$, the RG flow may linger near a real multicritical point or a pair of complex fixed points, producing walking or pseudocritical scaling with effective exponents $\nu_\star$ and $z_\star$, even though the thermodynamic transition is first order [28,29]. We define

$$x = (g - g_\star)L^{1/\nu_\star}, \qquad \beta = cL^{z_\beta}, \qquad z_\beta = z_\star, \tag{G1}$$

where $g_\star$ denotes the reference coupling about which the walking regime is organized. Within this finite-size

window, the symbols g_c, ν, and z used in the main-text pseudocritical ansatz correspond to $g_\star$, $\nu_\star$, and $z_\star$, respectively. We retain z_β to emphasize that the thermal trajectory is an input; choosing $z_\beta = z_\star$ keeps the pseudocritical tower at fixed temporal aspect ratio. The finite-size trace then contains two macroscopic branches, each dressed by a nontrivial low-energy tower.

1. Branch-resolved finite-size trace

Let $\alpha = 1, 2$ label the branches and m the levels within each branch. In the walking regime, we write

$$E_{\alpha m}(g, L) = L^d e_\alpha(g) + L^{-z_\star}\varepsilon_{\alpha m}(x) + \cdots. \tag{G2}$$

At inverse temperature $s\beta = scL^{z_\beta} = scL^{z_\star}$,

$$\begin{aligned} Z_\alpha(s\beta) &= \mathrm{e}^{-s\beta L^d e_\alpha(g)} Q_{\alpha,s}(x, c, L), \\ Q_{\alpha,s}(x, c, L) &\equiv Q_\alpha(sc, x) = \sum_m \mathrm{e}^{-sc\varepsilon_{\alpha m}(x)} + \cdots. \end{aligned} \tag{G3}$$

The full low-energy trace is

$$Z(s\beta) \simeq \mathrm{e}^{-s\beta L^d e_1(g)} Q_{1,s} + \mathrm{e}^{-s\beta L^d e_2(g)} Q_{2,s}. \tag{G4}$$

Unlike in the asymptotic first-order regime, $Q_{\alpha,s}$ are generally O(1) functions of both x and the temporal aspect ratio sc. They cannot be replaced by constant multiplicities.

2. Branch-symmetric common and relative sectors

A branch-symmetric decomposition follows from

$$\begin{aligned} \bar{e} &= \frac{e_1 + e_2}{2}, \qquad \Delta e = e_2 - e_1, \\ Q_{\mathrm{com},s} &= (Q_{1,s} Q_{2,s})^{1/2}, \qquad \delta_s = \frac{1}{2} \ln \frac{Q_{1,s}}{Q_{2,s}}. \end{aligned} \tag{G5}$$

Then, Eq. (G4) becomes

$$\begin{aligned} Z(s\beta) &= 2\mathrm{e}^{-s\beta L^d \bar{e}} Q_{\mathrm{com},s} \cosh Y_s + \cdots, \\ Y_s &= \frac{sc}{2} L^{d+z_\beta} \Delta e + \delta_s. \end{aligned} \tag{G6}$$

Interchanging the two branches sends $Y_s \mapsto -Y_s$ and leaves $Q_{\mathrm{com},s}$ invariant. The decomposition, therefore, does not privilege either branch.

To leading order, the second RTE is

$$\begin{aligned} S^{(2)} &= A_{\mathrm{com}}(x; c, L) + 2 \ln[2 \cosh Y_1] \\ &\quad - \ln[2 \cosh Y_2] + \cdots, \\ A_{\mathrm{com}}(x; c, L) &= 2 \ln Q_{\mathrm{com},1} - \ln Q_{\mathrm{com},2}. \end{aligned} \tag{G7}$$

The mean extensive branch energy $\bar{e}$ cancels exactly. By contrast, A_{com} is the RTE of the common multilevel tower and is generally a physical contribution. It may be neglected only when it is g independent over the fitted window, when symmetry forces its derivative to vanish, or when a background-subtracted observable is explicitly defined. A normalization convention alone cannot remove a g-dependent critical tower from the measured RTE.

The occupation of branch 2 in the $s\beta$ ensemble is

$$P_{2,s} = \frac{1}{1 + \mathrm{e}^{2Y_s}}, \qquad P_{1,s} = 1 - P_{2,s}. \tag{G8}$$

Differentiating Eq. (G7) yields

$$\partial_g S^{(2)} = \partial_g A_{\mathrm{com}} + 2 \tanh(Y_1) \partial_g Y_1 - \tanh(Y_2) \partial_g Y_2 + \cdots, \tag{G9}$$

with

$$\partial_g Y_s = \frac{sc}{2} L^{d+z_\beta} \Delta e'(g) + \frac{L^{1/\nu_\star}}{2} \partial_x \ln \frac{Q_{1,s}}{Q_{2,s}} + \cdots. \tag{G10}$$

Direct differentiation of Eq. (G4) gives the equivalent form

$$\begin{aligned} \partial_g S^{(2)} &= 2cL^{d+z_\beta} \Delta e'(g) [P_{2,2} - P_{2,1}] \\ &\quad + L^{1/\nu_\star} \left[2 \sum_{\alpha=1}^{2} P_{\alpha,1} \partial_x \ln Q_{\alpha,1} \right. \\ &\quad \left. - \sum_{\alpha=1}^{2} P_{\alpha,2} \partial_x \ln Q_{\alpha,2} \right] + \cdots. \end{aligned} \tag{G11}$$

Equation (G11) is the general leading-order result in the weakly first-order regime. The first line describes macroscopic transfer of weight between the two branches. The second contains both the response of the common critical tower and relative tower corrections. It scales as $L^{1/\nu_\star}$ within the walking regime and need not have the same line shape as the occupation-transfer term.

3. Single-mode reduction and the main-text form

When a single effective splitting controls the relative branch weight, Eq. (G11) reduces to a compact form. We parametrize

$$2Y_s = sX + \lambda + \cdots, \qquad X = cL^{d+z_\beta} \Delta e(g) + c\phi(x), \tag{G12}$$

where λ is a smooth, approximately s-independent relative multiplicity offset and $\phi(x)$ is the leading pseudocritical correction to the branch splitting. Then,

$$P_{2,s}(X) = \frac{1}{1 + \mathrm{e}^{sX + \lambda}}. \tag{G13}$$

Substituting Eq. (G12) into Eq. (G9) gives

$$\partial_g S^{(2)} = L^{1/\nu_\star}\partial_x A_{\rm com}(x;c,L) + \left[2cL^{d+z_\beta}\Delta e'(g) + 2cL^{1/\nu_\star}\phi'(x)\right] \times [P_{2,2}(X) - P_{2,1}(X)] + \cdots. \tag{G14}$$

The compact expression in the main text follows when the first line is negligible, forbidden by symmetry, or removed through an explicitly defined smooth-background subtraction. The correspondence between Eq. (G14) and main-text Eq. (32) is

$$y_{\rm main} \leftrightarrow X, \qquad p_s(y_{\rm main}) \leftrightarrow P_{2,s}(X), \quad \tilde{S}'_{\rm main}(x) \leftrightarrow 2c\phi'(x), \qquad z_\beta = z_\star. \tag{G15}$$

Thus, the variable y in the main-text occupation functions corresponds to the effective relative log-weight X, which includes both the macroscopic branch splitting and its leading pseudocritical correction. The two powers of L in the second line of Eq. (G14) arise from differentiating this same relative splitting. The first line is instead the independent RTE response of the common critical tower, a physical g-dependent multilevel contribution that cannot be removed by normalization alone.

For equal effective multiplicities, $\lambda = 0$, the occupation difference is

$$P_{2,2}(X) - P_{2,1}(X) = \frac{1}{1+e^{2X}} - \frac{1}{1+e^{X}} = \frac{e^X(1-e^X)}{(1+e^X)(1+e^{2X})}. \tag{G16}$$

This function vanishes as $X \to \pm\infty$, changes sign at $X = 0$, and has one extremum on each side. Unequal but s-independent multiplicities preserve the zero at $X = 0$ while making the two lobes asymmetric.

4. Zero crossing, crossover scales, and asymptotic recovery

We define the finite-size relative-coexistence point by

$$X[g_0(L), L] = 0. \tag{G17}$$

At this point $P_{2,2} = P_{2,1}$, and the occupation-transfer term in Eq. (G14) vanishes. The total DRTE is

$$\partial_g S^{(2)}|_{g_0(L)} = L^{1/\nu_\star}\partial_x A_{\rm com}(x_0;c,L) + \cdots. \tag{G18}$$

The occupation-transfer component, therefore, vanishes exactly at relative coexistence. At finite L, the full DRTE has an exact zero at the same point only if $\partial_x A_{\rm com}(x_0;c,L) = 0$.

If this derivative is parametrically smaller than the occupation-transfer slope, it produces only a subleading displacement of the zero. If the relative amplitudes have different s dependence, the condition $P_{2,2} = P_{2,1}$ may itself shift away from $X = 0$. In the asymptotic gapped two-branch regime, $Q_{\alpha,s}$ approach constants, $\partial_x A_{\rm com} \to 0$, and the exact first-order zero in Appendix F is recovered.

Within the single-mode regime, the two contributions to the relative prefactor define the amplitude scales

$$A_{\rm FO}(L) = 2c|\Delta e'(g_0)|L^{d+z_\beta}, \qquad A_\star(L) = 2c|\phi'(x_0)|L^{1/\nu_\star}. \tag{G19}$$

If $d + z_\beta > 1/\nu_\star$, their crossover estimate is

$$L_\times \sim \left[\frac{|\phi'(x_0)|}{|\Delta e'(g_0)|}\right]^{1/(d+z_\beta-1/\nu_\star)}. \tag{G20}$$

For $L \ll L_\times$, the lobe amplitude can grow as $L^{1/\nu_\star}$ even though coexistence produces its sign-changing shape. For $L \gg L_\times$, the branch-slope term proportional to L^{d+z_β} dominates. A common-tower contribution of the order of $L^{1/\nu_\star}$ can add a smooth offset or a single-peak component and must be included when interpreting the full line shape.

Expanding Eq. (G12) near $g_0(L)$ gives

$$X \simeq c\left[\Delta e'(g_0)L^{d+z_\beta} + \phi'(x_0)L^{1/\nu_\star}\right](g - g_0). \tag{G21}$$

The condition $|X| = O(1)$ then gives

$$\delta g_{\rm WFO} \sim \begin{cases} L^{-1/\nu_\star}, & L \ll L_\times, \\ L^{-(d+z_\beta)}, & L \gg L_\times, \end{cases} \tag{G22}$$

provided the walking description remains valid. For $L \gg \xi_\star$, the pseudocritical tower eventually freezes and the first-order scaling in Appendix F is recovered. An $L^{1/\nu_\star}$ collapse over accessible sizes, therefore, identifies a pseudocritical regime but does not by itself determine the thermodynamic order. The occupation-transfer contribution and its crossover must be examined concurrently.

APPENDIX H: UNIFIED INTERPRETATION, DIAGNOSTIC CRITERIA, AND RANGE OF VALIDITY

Equation (C10) compares the generalized force of the same finite-size Hamiltonian at inverse temperatures β and 2β. Throughout these appendixes, the sign convention is $S^{(2)} = 2\ln Z(\beta) - \ln Z(2\beta)$ and DRTE $= \partial_g S^{(2)}$, as fixed by Eq. (C4). The three transition classes are distinguished by the organization of the low-energy trace sampled by the two ensembles.

At a continuous transition, one critical tower controls the finite-size partition function:

$$S^{(2)} = \tilde{S}_2(x,c) + \cdots, \qquad \partial_g S^{(2)} = L^{1/\nu}\partial_x \tilde{S}_2(x,c) + \cdots, \quad x = (g-g_c)L^{1/\nu}. \tag{H1}$$

At fixed c, the leading RTE curves approach the common value $\tilde{S}_2(0,c)$ at $g = g_c$, with finite-size drift generated by irrelevant fields and metric factors. The DRTE scales as $L^{1/\nu}$, but no thermodynamic identity requires either a zero at g_c or a two-lobe profile. In the simulations, $c = \beta/L = 1$, while the metric-normalized temporal ratio is $\rho_\tau = v$.

At a standard first-order transition, two frozen gapped branches dominate:

$$\partial_g S^{(2)}_{\mathrm{FO}} = 2\beta\partial_g \Delta E(g,L)[p_2(y) - p_1(y)], \qquad y = \beta\Delta E. \tag{H2}$$

Consequently,

$$\partial_g S^{(2)}_{\mathrm{FO}} = L^{d+z_\beta}\mathcal{F}_2([g-g_0(L)]L^{d+z_\beta}; d_2/d_1) + \cdots. \tag{H3}$$

Under the assumptions in Appendix F, the occupation identity yields two opposite-sign lobes, an exact zero at the finite-size branch-energy crossing $g_0(L)$, a peak scale L^{d+z_β}, and a width $L^{-(d+z_\beta)}$. The zero need not coincide with the thermodynamic g_c until the crossing drift has vanished. The absolute RTE at coexistence is $\ln(d_1+d_2)$, rather than zero, unless a separate baseline is subtracted.

At a weakly first-order transition, coexistence is dressed by aspect-ratio-dependent pseudocritical towers. The general leading result is

$$\partial_g S^{(2)} = 2cL^{d+z_\beta}\Delta e'(g)[P_{2,2} - P_{2,1}] + L^{1/\nu_\star}\mathcal{B}(x,c,L) + \cdots, \tag{H4}$$

where

$$\mathcal{B} = 2\sum_\alpha P_{\alpha,1}\partial_x \ln Q_{\alpha,1} - \sum_\alpha P_{\alpha,2}\partial_x \ln Q_{\alpha,2}. \tag{H5}$$

The first line is the macroscopic occupation-transfer term and naturally generates a sign-changing two-lobe component. The second contains the common critical-tower response and relative tower corrections. For $L \lesssim \xi_\star$, it may add a smooth peak or offset, shift the zero of the full DRTE, or dominate its magnitude.

Under the additional single-relative-mode condition of Eq. (G12),

$$\partial_g S^{(2)} = L^{1/\nu_\star}\partial_x A_{\mathrm{com}} + \left[2cL^{d+z_\beta}\Delta e'(g) + 2cL^{1/\nu_\star}\phi'(x)\right] \times [P_{2,2} - P_{2,1}] + \cdots. \tag{H6}$$

Equation (G15) gives the dictionary to the compact main-text formula. That expression applies when $\partial_x A_{\mathrm{com}}$ is negligible, forbidden by symmetry, or explicitly removed as a smooth background. In this regime, the occupation component has a robust zero, and its two-lobe structure can coexist with apparent $L^{1/\nu_\star}$ peak scaling. An exact zero of the full finite-size DRTE requires $\partial_x A_{\mathrm{com}} = 0$ at the same point; a subleading but nonzero common-tower term shifts the zero by a finite-size correction.

These results sharpen the abbreviated statements in the main text. A collapse with an effective $\nu_\star$ signals an extended pseudocritical regime but does not by itself distinguish a continuous transition from a walking first-order transition. By contrast, a reproducible opposite-sign component governed by occupation transfer between the β and 2β ensembles provides evidence for competing spectral sectors. A generic smooth function can also display two extrema, so coexistence should be tested through the occupation identity, finite-size drift, aspect-ratio dependence, and robustness under smooth-background subtraction.

The spacetime Casimir interpretation is equally specific. Figure 1 compares one 2β cylinder with two disconnected β cylinders. After ultraviolet-local terms linear in the temporal circumference cancel, the remaining O(1) contribution is determined by the finite-aspect-ratio critical tower. The red curves schematically represent the change in infrared Matsubara spacing; they are neither exact many-body levels nor a mechanical force.

The formulas above assume that the low-temperature trace is dominated by the stated tower or branch structure. Corrections may arise from irrelevant fields, nonlinear scaling variables, a g-dependent velocity, finite-size crossing shifts, low-lying intrabranch modes, tunneling, interfaces, additional branches, or incomplete separation of common and relative tower sectors. Such effects modify drifts, offsets, and line shapes without changing the organizing hierarchy: a single critical tower, two frozen gapped branches, or two coexisting branches dressed by a long pseudocritical crossover.

APPENDIX I: APPLICATION TO THE SU(8) J_1-J_2 MODEL

We further test the DRTE diagnostic in the square-lattice SU(N) $J_1 - J_2 - Q$ model, which has been used in recent studies of SU(N) deconfined quantum criticality [22,37,101]. The model is defined on a bipartite square lattice, with SU(N) spins in the fundamental representation on one sublattice and in the conjugate representation on the other. Its Hamiltonian is

$$H = -\frac{J_1}{N}\sum_{\langle ij\rangle} P_{ij} - \frac{J_2}{N}\sum_{\langle\langle ij\rangle\rangle}\Pi_{ij} - \frac{Q}{N^2}\sum_{\langle i,j\rangle,\langle k,l\rangle} P_{ij}P_{kl}. \tag{I1}$$

Here, P_{ij} projects a nearest-neighbor pair on opposite sublattices into an SU(N) singlet, and Π_{ij} permutes the colors of two next-nearest-neighbor sites on the same sublattice. The J_1 term favors antiferromagnetic correlations, the J_2 term favors Néel order for large enough J_2/J_1, and the Q term is used mainly for smaller N to stabilize the VBS phase. For $N > 4$, the transition can be studied at $Q = 0$ by tuning $g = J_2/J_1$. In the following, we set the energy unit by $J_1 = 1$, take $N = 8$ and $Q = 0$, and tune g across the transition.

This model provides a useful test case because a recent entanglement entropy study suggested that the threshold value N_c separating weakly first-order behavior from a continuous SU(N) deconfined quantum critical point lies between $N = 7$ and $N = 8$ [37]. Thus, SU(8) is close to the proposed boundary and corresponds to a continuous phase transition. We do not aim here to determine N_c systematically. Instead, we use SU(8) as a focused test of whether the DRTE can detect a first-order component in a case where entanglement entropy scaling was interpreted as being compatible with a continuous transition.

The DRTE is obtained by evaluating this operator separately in the β and 2β ensembles. In this calculation, we use $\beta = 4L$, so that the two ensembles entering DRTE are sampled at $\beta = 4L$ and $2\beta = 8L$. This choice is used to reduce residual finite-temperature effects in the subtraction. The data shown below are obtained for $L = 16, 24, 32$ over the same coupling range $0.7 \le g \le 2.0$.

Figure 7(a) shows the DRTE $\partial S^{(2)}/\partial g$ as a function of g. The curves show a sign-changing structure around the transition: DRTE develops a negative peak on the smaller-g side, crosses zero near the transition point, and then forms a positive peak on the larger-g side. This behavior is the characteristic shape of a first-order transition in our protocol. It is different from the single-peak scaling form of a continuous transition. In Fig. 7(b), we did the data collapse with the form

$$\partial S^{(2)}/\partial g/L^{1/\nu} = \mathcal{F}\left[(g - g_c)L^{1/\nu}\right] + b/L. \tag{I2}$$

The collapse gives

$$g_c = 1.17(4), \qquad \nu = 0.67(4). \tag{I3}$$

In the present context, ν should be understood as an effective pseudocritical exponent in the accessible finite-size regime rather than as independent evidence for a stable continuous fixed point. The diagnostic information comes from the combination of the collapse in Fig. 7(b) and the sign-changing DRTE profile in Fig. 7(a).

These results indicate that the transition in the SU(8) J_1-J_2 model still shows weakly first-order behavior. This differs from the interpretation based on smooth-boundary entanglement entropy scaling, where SU(8) was placed at or above the proposed onset of continuous behavior [37]. The SU(8) data show that the DRTE can reveal a first-order component with modest system sizes in a case where the transition is difficult to settle using other finite-size probes.

APPENDIX J: BINDER CUMULANT AND CORRELATION FUNCTIONS FOR THE J-Q_2 MODEL

To further illustrate the practical advantage of our method, we have added a comparison with conventional observables for the J-Q_2 model (see Fig. 8). The Binder cumulant computed up to $L = 256$ shows no negative values that would indicate a first-order transition. The spin and dimer correlation functions measured at the largest separation, even with system sizes up to $L = 384$, do not display a clear tendency to converge to finite constants in

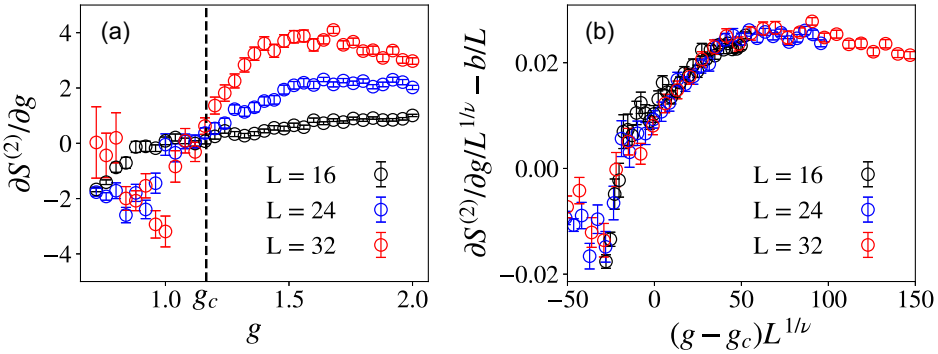
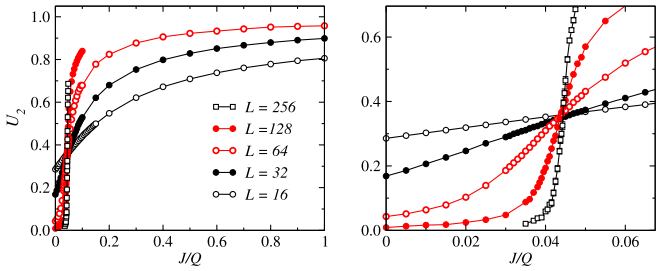
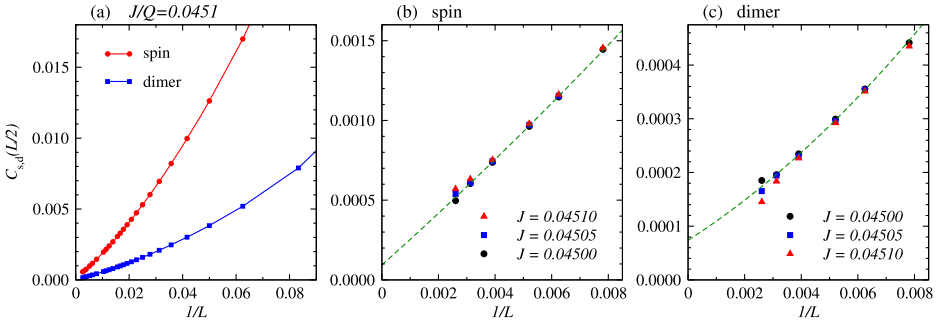


FIG. 7. Application to the square-lattice SU(8) J_1-J_2 model. Here, $g = J_2/J_1$, and the inverse temperature is fixed to $\beta = 4L$; the two thermal ensembles entering the DRTE are, therefore, sampled at $\beta = 4L$ and $2\beta = 8L$. (a) DRTE $\partial S^{(2)}/\partial g$ for $L = 16, 24, 32$ in the range $0.7 \le g \le 2.0$. The vertical dashed line marks the fitted transition point, $g_c = 1.17(4)$. The negative and positive lobes around g_c, together with the zero crossing, are the finite-size coexistence signature expected for a first-order transition. (b) Data collapse of the same data using $(g - g_c)L^{1/\nu}$ and $\partial S^{(2)}/\partial g/L^{1/\nu} - b/L$, with $g_c = 1.17(4)$ and $\nu = 0.67(4)$. The collapse captures the pseudocritical scaling regime.



(a) Binder cumulant of the J-Q_2 model



(b) Spin and dimer correlations at distance $L/2$

FIG. 8. (a) Binder cumulant of the J-Q_2 model [5,39]. The left panel shows results up to $J/Q = 1$, where U_2 approaches 1, indicating a Néel state. For smaller J/Q, the cumulant vanishes with increasing size, demonstrating a nonmagnetic state for $J/Q < 0.045$. The cumulant remains positive for all J/Q, showing no phase coexistence; i.e., the transition is continuous based on these results. (b) Spin and dimer correlation functions at distance $L/2$ vs the inverse system size in the critical J-Q_2 model, obtained with QMC calculations [31]. Both correlation functions are shown vs $1/L$, with L from 16 (spin) or 12 (dimer) up to $L = 384$. The green dashed curves are cubic collective fits to the data.

the thermodynamic limit, making it impossible to unambiguously identify phase coexistence. In stark contrast, our DRTE already provides a definitive, qualitative signature of the weakly first-order transition at system sizes as small as $L = 56$. It is also worth noting that the computational cost of standard QMC calculations scales as $\beta L^2 \sim L^3$. This implies that, even with roughly 300 times the computational effort required for our $L = 56$ DRTE result, the conventional diagnostics still cannot conclusively characterize the nature of the transition, whereas our method does so cleanly and with minimal computational expense.

APPENDIX K: TENSOR-NETWORK IMPLEMENTATION OF RÉNYI THERMAL ENTROPY

The numerical results presented in the main text were obtained primarily using quantum Monte Carlo simulations. Here, we demonstrate that the RTE framework is not restricted to a particular numerical method. As a proof of principle, we implement the RTE using a thermal tensor-network method for the one-dimensional transverse-field Ising model:

$$H = -J\sum_i \sigma_i^z \sigma_{i+1}^z - h\sum_i \sigma_i^x. \tag{K1}$$

This model provides a particularly clean benchmark because its critical point and critical exponent are exactly known:

$$h_c = J, \qquad \nu = 1. \tag{K2}$$

A thermal tensor-network calculation provides access to the finite-temperature density operator $e^{-\beta H}$ and, hence, to the partition function

$$Z(\beta) = \mathrm{Tr} e^{-\beta H}. \tag{K3}$$

The Rényi thermal entropy can, therefore, be calculated directly from

$$S^{(n)} = \frac{1}{1-n}[\ln Z(n\beta) - n \ln Z(\beta)], \tag{K4}$$

which is exactly the same quantity used in the quantum Monte Carlo implementation discussed in the main text.

For the transverse-field Ising model, the dynamical exponent is $z = 1$, and we choose $\beta = L$. Near the quantum critical point, the RTE obeys the continuous-transition scaling form

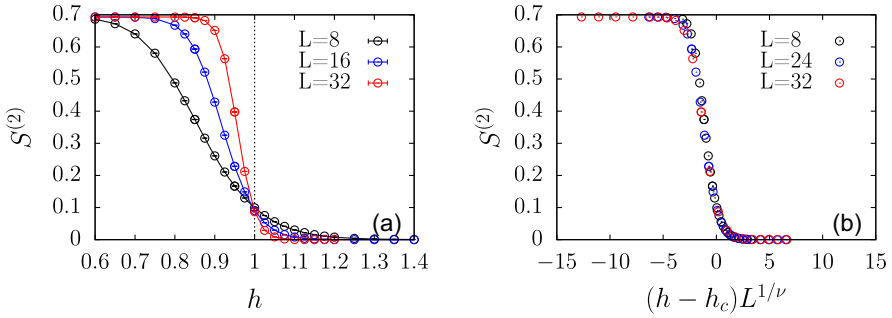


FIG. 9. (a) Second-order RTE and (b) the corresponding data collapse near the quantum critical point of the one-dimensional transverse-field Ising model [(1 + 1)D Ising universality class]. The Hamiltonian is $H = -J\sum_i \sigma_i^z\sigma_{i+1}^z - h\sum_i \sigma_i^x$, with $J = 1$ fixed and h serving as the tuning parameter. Applying the continuous-transition scaling form derived in the main text, we obtain a critical field $h_c = 0.99(1)$ and a critical exponent $\nu = 1.05(6)$, consistent within error bars with the exact results $h_c = 1$ and $\nu = 1$. All numerical results were obtained using the thermal tensor-network method [92,94].

$$S^{(2)} = \tilde{S}\left[(h-h_c)L^{1/\nu}\right] + \cdots. \tag{K5}$$

As shown in Fig. 9(a), the RTE curves for different system sizes exhibit a clear crossing near the quantum critical point. Applying Eq. (K5), we obtain

$$h_c = 0.99(1), \qquad \nu = 1.05(6), \tag{K6}$$

which agree with the exact results $h_c = 1$ and $\nu = 1$ within the numerical uncertainty. The corresponding data collapse is shown in Fig. 9(b).

The DRTE can be evaluated within the same thermal tensor-network framework. For a general tuning parameter g in the Hamiltonian,

$$\frac{\partial S^{(n)}}{\partial g} = \frac{1}{1-n}\left[-n\beta\left\langle\frac{\partial H}{\partial g}\right\rangle_{n\beta} + n\beta\left\langle\frac{\partial H}{\partial g}\right\rangle_{\beta}\right], \tag{K7}$$

where the two expectation values are evaluated using the thermal density matrices at inverse temperatures $n\beta$ and β, respectively. Thus, both the RTE and DRTE can be implemented directly within finite-temperature tensor-network calculations.

We emphasize that the transverse-field Ising example is intended as a benchmark demonstrating the numerical portability of the RTE framework rather than as an independent tensor-network realization of a weakly first-order transition. The weakly first-order theory developed in the main text is formulated directly in terms of the finite-size partition function and, therefore, does not depend on whether the partition function is evaluated using quantum Monte Carlo, tensor networks, or another numerical method.

In particular, when two competing thermodynamic branches contribute appreciably to the finite-size partition function,

$$Z(s\beta) \simeq Z_1(s\beta) + Z_2(s\beta), \tag{K8}$$

the DRTE probes how their relative statistical weights differ between the β and $n\beta$ ensembles. Therefore, the same two-branch mechanism derived in the main text predicts a zero crossing and an opposite-sign double-peak structure in a tensor-network calculation of a weakly first-order transition.

The advantage of the RTE framework emerges once the system enters the low-energy regime. The Rényi combination

$$S^{(n)} = \frac{1}{1-n}\left[\ln Z(n\beta) - n\ln Z(\beta)\right] \tag{K9}$$

cancels the dominant smooth contribution that is linear in the imaginary-time extent. Consequently, the universal or coexistence-controlled finite-size contribution becomes more directly visible. This mechanism is independent of the numerical technique used to evaluate the partition functions.

Therefore, the transverse-field Ising calculation presented here serves as a controlled benchmark showing that the RTE finite-size scaling framework can be implemented using thermal tensor networks and correctly reproduces known critical properties. The same partition-function-based construction and weakly first-order scaling theory can be applied to tensor-network calculations of more general quantum many-body systems.

[1] S. Sachdev, *Quantum phase transitions*, Phys. World **12**, 33 (1999).
[2] G. H. Wannier, *Statistical Physics* (Courier Corporation, New York, 1987).
[3] S. M. Girvin and K. Yang, *Modern Condensed Matter Physics* (Cambridge University Press, Cambridge, England, 2019).
[4] T. Senthil, A. Vishwanath, L. Balents, S. Sachdev, and M. P. Fisher, *Deconfined quantum critical points*, Science **303**, 1490 (2004).

[5] A. W. Sandvik, *Evidence for deconfined quantum criticality in a two-dimensional Heisenberg model with four-spin interactions*, Phys. Rev. Lett. **98**, 227202 (2007).

[6] A. W. Sandvik, *Continuous quantum phase transition between an antiferromagnet and a valence-bond solid in two dimensions: Evidence for logarithmic corrections to scaling*, Phys. Rev. Lett. **104**, 177201 (2010).

[7] A. Nahum, P. Serna, J. T. Chalker, M. Ortuño, and A. M. Somoza, *Emergent SO(5) symmetry at the néel to valence-bond-solid transition*, Phys. Rev. Lett. **115**, 267203 (2015).

[8] N. Ma, G.-Y. Sun, Y.-Z. You, C. Xu, A. Vishwanath, A. W. Sandvik, and Z. Y. Meng, *Dynamical signature of fractionalization at a deconfined quantum critical point*, Phys. Rev. B **98**, 174421 (2018).

[9] H. Shao, W. Guo, and A. W. Sandvik, *Quantum criticality with two length scales*, Science **352**, 213 (2016).

[10] C. Wang, A. Nahum, M. A. Metlitski, C. Xu, and T. Senthil, *Deconfined quantum critical points: Symmetries and dualities*, Phys. Rev. X **7**, 031051 (2017).

[11] T. Senthil, *Deconfined quantum critical points: A review*, *50 Years of the Renormalization Group: Dedicated to the Memory of Michael E Fisher* edited by A. Aharony, O. Entin-Wohlman, D. A. Huse, and L. Radzihovsky (World Scientific, Singapore, 2024), p. 169, 10.1142/9789811282386_0014.

[12] B.-B. Mao, Z. Wang, B.-B. Chen, and Z. Yan, *Detecting the emergent continuous symmetry of criticality via a subsystem's entanglement spectrum*, Phys. Rev. Lett. **136**, 046401 (2026).

[13] S. Yang, F. Xu, D.-C. Lu, Y.-Z. You, H.-Q. Lin, and X.-J. Yu, *Deconfined criticality as intrinsically gapless topological state in one dimension*, Phys. Rev. B **113**, L201105 (2026).

[14] Y. Liu, T. Sato, D. Hou, Z. Wang, W. Guo, and F. F. Assaad, *Edge modes of topological Mott insulators and deconfined quantum critical points*, arXiv:2508.04455.

[15] R. Ma and C. Wang, *Theory of deconfined pseudocriticality*, Phys. Rev. B **102**, 020407(R) (2020).

[16] D.-C. Lu, *Nonlinear sigma model description of deconfined quantum criticality in arbitrary dimensions*, SciPost Phys. Core **6**, 047 (2023).

[17] Z. Wang, M. P. Zaletel, Roger S. K. Mong, and F. F. Assaad, *Phases of the* $(2+1)$ *dimensional so(5) nonlinear sigma model with topological term*, Phys. Rev. Lett. **126**, 045701 (2021).

[18] Z. Zhou, L. Hu, W. Zhu, and Y.-C. He, *The SO(5) deconfined phase transition under the fuzzy sphere microscope: Approximate conformal symmetry, pseudo-criticality, and operator spectrum*, Phys. Rev. X **14**, 021044 (2024).

[19] J. Zhao, Y.-C. Wang, Z. Yan, M. Cheng, and Z. Y. Meng, *Scaling of entanglement entropy at deconfined quantum criticality*, Phys. Rev. Lett. **128**, 010601 (2022).

[20] J. D'Emidio and A. W. Sandvik, *Entanglement entropy and deconfined criticality: emergent SO(5) symmetry and proper lattice bipartition*, Phys. Rev. Lett. **133**, 166702 (2024).

[21] Z. Deng, L. Liu, W. Guo, and H.-Q. Lin, *Diagnosing quantum phase transition order and deconfined criticality via entanglement entropy*, Phys. Rev. Lett. **133**, 100402 (2024).

[22] J. Lou, A. W. Sandvik, and N. Kawashima, *Antiferromagnetic to valence-bond-solid transitions in two-dimensional su (n) Heisenberg models with multispin interactions*, Phys. Rev. B **80**, 180414(R) (2009).

[23] Z. Wang, Z. Deng, Z. Liu, Z. Wang, Y.-M. Ding, L. Zhang, W. Guo, and Z. Yan, *Universal behavior in entanglement entropy reveals quantum criticality and underlying symmetry breaking*, Chin. Phys. Lett. **42**, 110712 (2025).

[24] Y. Liu, Z. Wang, T. Sato, M. Hohenadler, C. Wang, W. Guo, and F. F. Assaad, *Superconductivity from the condensation of topological defects in a quantum spin-hall insulator*, Nat. Commun. **10**, 2658 (2019).

[25] Y. D. Liao, X. Y. Xu, Z. Y. Meng, and Y. Qi, *Dirac fermions with Plaquette interactions. I. SU(2) phase diagram with gross-neveu and deconfined quantum criticalities*, Phys. Rev. B **106**, 075111 (2022).

[26] X.-F. Zhang, Y.-C. He, S. Eggert, R. Moessner, and F. Pollmann, *Continuous easy-plane deconfined phase transition on the kagome lattice*, Phys. Rev. Lett. **120**, 115702 (2018).

[27] D.-X. Liu, Z. Xiong, Y. Xu, and X.-F. Zhang, *Deconfined quantum phase transition on the kagome lattice: Distinct velocities of spinon and string excitations*, Phys. Rev. B **109**, L140404 (2024).

[28] V. Gorbenko, S. Rychkov, and B. Zan, *Walking, weak first-order transitions, and complex CFTs*, J. High Energy Phys. 10 (2018) 108.

[29] V. Gorbenko, S. Rychkov, and B. Zan, *Walking, weak first-order transitions, and complex CFTs II. Two-dimensional Potts model at* $q > 4$, SciPost Phys. **5**, 050 (2018).

[30] Y. Tang, Q. Liu, Q. Tang, and W. Zhu, *Boundary criticality of complex conformal field theory: A case study in the non-hermitian 5-state Potts model*, SciPost Phys. **19**, 164 (2025).

[31] J. Takahashi, H. Shao, B. Zhao, W. Guo, and A. W. Sandvik, *SO(5) multicriticality in two-dimensional quantum magnets*, arXiv:2405.06607.

[32] B.-B. Chen, X. Zhang, Y. Wang, K. Sun, and Z. Y. Meng, *Phases of* $(2+1)$ *d so (5) nonlinear sigma model with a topological term on a sphere: Multicritical point and disorder phase*, Phys. Rev. Lett. **132**, 246503 (2024).

[33] W.-Y. Liu, J. Hasik, S.-S. Gong, D. Poilblanc, W.-Q. Chen, and Z.-C. Gu, *Emergence of gapless quantum spin liquid from deconfined quantum critical point*, Phys. Rev. X **12**, 031039 (2022).

[34] Y. Zhu, Z. Liu, Z. Wang, Y.-C. Wang, and Z. Yan, *Bipartite entanglement and surface criticality: The extra contribution of the nonordinary edge in entanglement*, Phys. Rev. Lett. **136**, 046501 (2026).

[35] Z. Wang, C. Guo, B.-B. Mao, and Z. Yan, *Universal and non-universal contributions of entanglement under different bipartitions*, arXiv:2601.12365.

[36] Y. Zhu, Z. Wang, M. Cheng, and Z. Yan, *Criticality on Rényi defects at* $(2+1)$ *d o (3) quantum critical points*, Phys. Rev. Lett. **137**, 156501 (2026).

[37] M. Song, J. Zhao, M. Cheng, C. Xu, M. Scherer, L. Janssen, and Z. Y. Meng, *Evolution of entanglement entropy at su (n) deconfined quantum critical points*, Sci. Adv. **11**, eadr0634 (2025).

[38] M. E. Fisher and M. N. Barber, *Scaling theory for finite-size effects in the critical region*, Phys. Rev. Lett. **28**, 1516 (1972).

[39] A. W. Sandvik, *Computational studies of quantum spin systems*, AIP Conf. Proc. **1297**, 135 (2010).

[40] K. G. Wilson, *Renormalization group and critical phenomena. I. Renormalization group and the Kadanoff scaling picture*, Phys. Rev. B **4**, 3174 (1971).

[41] H. B. G. Casimir, *On the attraction between two perfectly conducting plates*, Proc. K. Ned. Akad. Wet. **51**, 793 (1948).

[42] G. Plunien, B. Müller, and W. Greiner, *The Casimir effect*, Phys. Rep. **134**, 87 (1986).

[43] K. A. Milton, *The Casimir Effect: Physical Manifestations of Zero-Point Energy* (World Scientific, Singapore, 2001).

[44] M. E. Fisher and P.-G. de Gennes, *Phénomènes aux parois dans un mélange binaire critique*, C. R. Acad. Sci. Paris B **287**, 207 (1978).

[45] M. Krech, *The Casimir Effect in Critical Systems* (World Scientific, Singapore, 1994).

[46] J. L. Cardy and I. Peschel, *Finite-size dependence of the free energy in two-dimensional critical systems*, Nucl. Phys. **B300**, 377 (1988).

[47] S. Ma, H. Miao, Y. Xiang, and S. Zhang, *Enhanced dynamic Casimir effect in temporally and spatially modulated Josephson transmission line*, Laser Photonics Rev. **13**, 1900164 (2019).

[48] A. Rényi, *On measures of entropy and information*, in *Proceedings of the Fourth Berkeley Symposium on Mathematical Statistics and Probability, Volume 1: Contributions to the Theory of Statistics* (University of California Press, Berkeley, California, 1961), Vol. 1, pp. 547–561.

[49] M. Ozawa and N. Javerzat, *Perspective on physical interpretations of Rényi entropy in statistical mechanics*, Europhys. Lett. **147**, 11001 (2024).

[50] J. C. Baez, *Rényi entropy and free energy*, Entropy **24**, 706 (2022).

[51] L. Amico, R. Fazio, A. Osterloh, and V. Vedral, *Entanglement in many-body systems*, Rev. Mod. Phys. **80**, 517 (2008).

[52] J. Eisert, M. Cramer, and M. B. Plenio, *Colloquium: Area laws for the entanglement entropy*, Rev. Mod. Phys. **82**, 277 (2010).

[53] N. Laflorencie, *Quantum entanglement in condensed matter systems*, Phys. Rep. **646**, 1 (2016).

[54] B. Zeng, X. Chen, D.-L. Zhou, and X.-G. Wen, *Quantum Information Meets Quantum Matter: From Quantum Entanglement to Topological Phases of Many-Body Systems*, Quantum Science and Technology (Springer, New York, 2019), 10.1007/978-1-4939-9084-9.

[55] Z. Wang, Z. Wang, Y.-M. Ding, B.-B. Mao, and Z. Yan, *Bipartite reweight-annealing algorithm to extract large-scale data of entanglement entropy and its derivative in high precision*, Nat. Commun. **16**, 5880 (2025).

[56] Y.-M. Ding, Y. Tang, Z. Wang, Z. Wang, B.-B. Mao, and Z. Yan, *Tracking the variation of entanglement rényi negativity: A quantum Monte Carlo study*, Phys. Rev. B **111**, L241108 (2025).

[57] Z. Wang, Z. Liu, B.-B. Mao, Z. Wang, and Z. Yan, *Addressing general measurements in quantum Monte Carlo*, Nat. Commun. **17**, 679 (2026).

[58] A. W. Sandvik, *Stochastic series expansion method with operator-loop update*, Phys. Rev. B **59**, R14157 (1999).

[59] A. W. Sandvik, *Stochastic series expansion methods*, arXiv:1909.10591.

[60] O. F. Syljuåsen and A. W. Sandvik, *Quantum Monte Carlo with directed loops*, Phys. Rev. E **66**, 046701 (2002).

[61] Z. Yan, Y. Wu, C. Liu, O. F. Syljuåsen, J. Lou, and Y. Chen, *Sweeping cluster algorithm for quantum spin systems with strong geometric restrictions*, Phys. Rev. B **99**, 165135 (2019).

[62] Z. Yan, *Global scheme of sweeping cluster algorithm to sample among topological sectors*, Phys. Rev. B **105**, 184432 (2022).

[63] K.-H. Wu, T.-C. Lu, C.-M. Chung, Y.-J. Kao, and T. Grover, *Entanglement Renyi negativity across a finite temperature transition: A Monte Carlo study*, Phys. Rev. Lett. **125**, 140603 (2020).

[64] Y.-M. Ding, J.-S. Sun, N. Ma, G. Pan, C. Cheng, and Z. Yan, *Reweight-annealing method for evaluating the partition function via quantum Monte Carlo calculations*, Phys. Rev. B **110**, 165152 (2024).

[65] Z. Dai and X. Y. Xu, *Residual entropy from the temperature incremental Monte Carlo method*, Phys. Rev. B **111**, L081108 (2025).

[66] N. Ma, J.-S. Sun, G. Pan, C. Cheng, and Z. Yan, *Defining a universal sign to strictly probe a phase transition*, Phys. Rev. B **110**, 125141 (2024).

[67] S. Wu, X. Ran, B. Yin, Q.-F. Li, B.-B. Mao, Y.-C. Wang, and Z. Yan, *Classical model emerges in quantum entanglement: Quantum Monte Carlo study for an Ising-Heisenberg bilayer*, Phys. Rev. B **107**, 155121 (2023).

[68] R. Guida and J. Zinn-Justin, *Critical exponents of the N-vector model*, J. Phys. A **31**, 8103 (1998).

[69] Y. Deng and Henk W. J. Blöte, *Simultaneous analysis of several models in the three-dimensional Ising universality class*, Phys. Rev. E **68**, 036125 (2003).

[70] A. Pelissetto and E. Vicari, *Critical phenomena and renormalization-group theory*, Phys. Rep. **368**, 549 (2002).

[71] M. Campostrini, M. Hasenbusch, A. Pelissetto, P. Rossi, and E. Vicari, *Critical behavior of the three-dimensional XY universality class*, Phys. Rev. B **63**, 214503 (2001).

[72] M. Campostrini, M. Hasenbusch, A. Pelissetto, P. Rossi, and E. Vicari, *Critical exponents and equation of state of the three-dimensional Heisenberg universality class*, Phys. Rev. B **65**, 144520 (2002).

[73] Y. Deng, Henk W. J. Blöte, and M. P. Nightingale, *Surface and bulk transitions in three-dimensional* $\mathrm{O}(n)$ *models*, Phys. Rev. E **72**, 016128 (2005).

[74] M. Matsumoto, C. Yasuda, S. Todo, and H. Takayama, *Ground-state phase diagram of quantum Heisenberg antiferromagnets on the anisotropic dimerized square lattice*, Phys. Rev. B **65**, 014407 (2001).

[75] C. Ding, L. Zhang, and W. Guo, *Engineering surface critical behavior of* $(2+1)$*-dimensional o (3) quantum critical points*, Phys. Rev. Lett. **120**, 235701 (2018).

[76] W. Zhu, C. Ding, L. Zhang, and W. Guo, *Exotic surface behaviors induced by geometrical settings of the two-dimensional dimerized quantum XXZ model*, arXiv:2111.12336.
[77] Z. Deng, L. Liu, W. Guo, and H. Q. Lin, *Improved scaling of the entanglement entropy of quantum antiferromagnetic Heisenberg systems*, Phys. Rev. B **108**, 125144 (2023).
[78] B.-B. Mao, Y.-M. Ding, Z. Wang, S. Hu, and Z. Yan, *Sampling reduced density matrix to extract fine levels of entanglement spectrum and restore entanglement Hamiltonian*, Nat. Commun. **16**, 2880 (2025).
[79] K. Binder and D. P. Landau, *Finite-size scaling at first-order phase transitions*, Phys. Rev. B **30**, 1477 (1984).
[80] B. Zhao, P. Weinberg, and A. W. Sandvik, *Symmetry-enhanced discontinuous phase transition in a two-dimensional quantum magnet*, Nat. Phys. **15**, 678+ (2019).
[81] T. Senthil, L. Balents, S. Sachdev, A. Vishwanath, and Matthew P. A. Fisher, *Quantum criticality beyond the Landau-Ginzburg-Wilson paradigm*, Phys. Rev. B **70**, 144407 (2004).
[82] R. G. Melko and R. K. Kaul, *Scaling in the fan of an unconventional quantum critical point*, Phys. Rev. Lett. **100**, 017203 (2008).
[83] R. K. Kaul, *Quantum criticality in SU(3) and SU(4) antiferromagnets*, Phys. Rev. B **84**, 054407 (2011).
[84] A. Nahum, J. T. Chalker, P. Serna, M. Ortuño, and A. M. Somoza, *Deconfined quantum criticality, scaling violations, and classical loop models*, Phys. Rev. X **5**, 041048 (2015).
[85] Y. Nakayama and T. Ohtsuki, *Necessary condition for emergent symmetry from the conformal bootstrap*, Phys. Rev. Lett. **117**, 131601 (2016).
[86] B. Zhao, J. Takahashi, and A. W. Sandvik, *Multicritical deconfined quantum criticality and Lifshitz point of a helical valence-bond phase*, Phys. Rev. Lett. **125**, 257204 (2020).
[87] D.-C. Lu, C. Xu, and Y.-Z. You, *Self-duality protected multicriticality in deconfined quantum phase transitions*, Phys. Rev. B **104**, 205142 (2021).
[88] A. B. Kuklov, M. Matsumoto, N. V. Prokof'ev, B. V. Svistunov, and M. Troyer, *Deconfined criticality: Generic first-order transition in the SU(2) symmetry case*, Phys. Rev. Lett. **101**, 050405 (2008).
[89] K. Chen, Y. Huang, Y. Deng, A. B. Kuklov, N. V. Prokof'ev, and B. V. Svistunov, *Deconfined criticality flow in the Heisenberg model with ring-exchange interactions*, Phys. Rev. Lett. **110**, 185701 (2013).
[90] Y. D. Liao, G. Pan, W. Jiang, Y. Qi, and Z. Y. Meng, *The teaching from entanglement: 2d SU(2) antiferromagnet to valence bond solid deconfined quantum critical points are not conformal*, arXiv:2302.11742.
[91] M. Song, J. Zhao, Z. Y. Meng, C. Xu, and M. Cheng, *Extracting subleading corrections in entanglement entropy at quantum phase transitions*, SciPost Phys. **17**, 010 (2024).
[92] Q. Li, Y. Gao, Y.-Y. He, Y. Qi, B.-B. Chen, and W. Li, *Tangent space approach for thermal tensor network simulations of the 2D Hubbard model*, Phys. Rev. Lett. **130**, 226502 (2023).
[93] Y.-C. Wang, N. Ma, M. Cheng, and Z. Y. Meng, *Scaling of the disorder operator at deconfined quantum criticality*, SciPost Phys. **13**, 123 (2022).
[94] B.-B. Chen, L. Chen, Z. Chen, W. Li, and A. Weichselbaum, *Exponential thermal tensor network approach for quantum lattice models*, Phys. Rev. X **8**, 031082 (2018).
[95] R. M. Neal, *Annealed importance sampling*, Stat. Comput. **11**, 125 (2001).
[96] How to measure the energy in SSE has been carefully explained in Professor Sandvik's tutorial https://physics.bu.edu/~sandvik/programs/ssebasic/ssebasic.html.
[97] S. Sachdev, *Quantum Phase Transitions* (Cambridge University Press, Cambridge, England, 2011).
[98] M. Campostrini, A. Pelissetto, and E. Vicari, *Finite-size scaling at quantum transitions*, Phys. Rev. B **89**, 094516 (2014).
[99] P. W. Anderson, *An approximate quantum theory of the antiferromagnetic ground state*, Phys. Rev. **86**, 694 (1952).
[100] H. Watanabe, *Counting rules of Nambu–Goldstone modes*, Annu. Rev. Condens. Matter Phys. **11**, 169 (2020).
[101] R. K. Kaul and A. W. Sandvik, *Lattice model for the* SU(n) *Néel to valence-bond solid quantum phase transition at large n*, Phys. Rev. Lett. **108**, 137201 (2012).